Installed performance evaluation of an air turbo-rocket expander engine

V. Fernández-Villacé [a,*], G. Paniagua [a], J. Steelant [b]

[a] *Von Karman Institute for Fluid Dynamics, Chaussée de Waterloo 72, Rhode-St-Genèse, Belgium*
[b] *European Space Agency, Keplerlaan 1, Noordwijk, The Netherlands*

ABSTRACT

The propulsion plant of a prospective supersonic cruise aircraft consists of an air turbo-rocket expander and a dual-mode ramjet. A comprehensive numerical model was constructed to examine the performance of the air turbo-rocket during the supersonic acceleration of the vehicle. The numerical model comprised a one-dimensional representation of the fluid paths through the dual-mode ramjet, the air turbo-rocket combustor, the regenerator and the airframe-integrated nozzle, whereas the turbomachinery and the air turbo-rocket bypass were included as zero-dimensional models. The intake operation was based on the results of time-averaged Euler simulations. A preliminary engine analysis revealed that the installation effects restricted significantly the operational envelope, which was subsequently extended bypassing the air turbo-rocket. Hence the engine was throttled varying the mixture ratio and the fan compression ratio. Nevertheless, the performance was optimal when the demand from the air turbo-rocket matched the intake air flow capture. The heat recovery across the regenerator was found critical for the operation of the turbomachinery at low speed. The transition of the air turbo-rocket to ramjet operation was identified at Mach 4.5. During this regime, the propulsion plant was rather insensitive to the mixture ratio and was throttled with the air turbo-rocket throat area.

© 2014 Elsevier Masson SAS. All rights reserved.

1. Introduction

The air turbo-rocket expander under investigation is sought as the acceleration engine for a Mach 8 cruise aircraft [28,29]. The mission of the air turbo-rocket engine is to accelerate from take-off to Mach 4.5 at 24 km of altitude, where a dual-mode ramjet (DMR) accelerates further to cruise speed [20]. The hydrogen-fueled propulsion plant consists of six air turbo-rockets and a dual-mode ramjet mounted in parallel and highly integrated within the airframe. The use of the terms air turbo-rocket and air turbo-ramjet is often subject to controversy in the literature. Following the distinction made by Kozlaykov [19], the gas generator of an air turbo-ramjet follows a Brayton cycle, whereas the fuel across the heat exchanger and the turbine which powers the fan follows a Rankine cycle in the air turbo-rocket. In this sense, referring to the air turbo-rocket as expander is redundant, but serves to distinguish from the air turbo-rocket with gas generator, a term frequently used to designate the air turbo-ramjet. Each of the two engine bays, sideways of the aircraft, comprise three air turbo-rockets, Fig. 1. The turbomachinery of each air turbo-rocket ex-

pander consists of a two-stage counter-rotating fan and a hydrogen pump driven by a counter-rotating hydrogen turbine. The turbine is modeled as a single unit despite that different stages drive the pump and the fan, depicted in Fig. 2. The identification of the control inputs and the performance of the power plant is essential for the evaluation of the aircraft mission and, in addition, for the design of the aircraft flight controller [34]. In this respect, the air turbo-rocket cycle which best meets the mission requirements of the aircraft was identified in a previous study by Rodríguez-Miranda et al. [27]. Nonetheless, the uninstalled performances (integration effects were neglected) of the air turbo-rocket which resulted from that previous analysis did not suffice to assess the aircraft mission.

An extended model addressing the integral propulsion plant of the aircraft, i.e. both high and low speed inlets, bleeding system, air turbo-rockets, dual-mode ramjet, regenerator and the airframe-embedded nozzle, was developed in order to compute the installed performances in the supersonic regime. The model was based on EcosimPro [32] and the set of libraries of the European Space Propulsion System Simulation (ESPSS) [10,25]. Ad hoc models of the nozzle, the dual-mode ramjet, the air turbo-rocket bypass system and the regenerator were developed. The one-dimensional flow through the dual-mode ramjet, the

* Corresponding author. Tel.: +32 2359 9611; fax: +32 2359 9600.
E-mail address: villace@vki.ac.be (V. Fernández-Villacé).

Nomenclature

A	transversal area	m^2
a	speed of sound	$m\,s^{-1}$
B	bypass ratio	
C_p	heat capacity at constant pressure	$m^2\,s^{-2}\,K^{-1}$
C_x	spillage drag coefficient	
D_h	hydraulic diameter	m
e	total energy: $e = h^0 - pv$	$m^2\,s^{-2}$
G	Gibbs potential	$kg\,m^2\,s^{-2}$
h	enthalpy	$m^2\,s^{-2}$
I_{sp}	specific impulse	$m\,s^{-1}$
k	thermal conductivity	$kg\,m\,s^{-3}\,K^{-1}$
	or sensitivity	
N	number of moles	mol
p	pressure	$kg\,m^{-1}\,s^{-2}$
R_g	ideal gas constant	$m^2\,s^{-2}\,K^{-1}$
T	temperature	K
T_{sp}	specific thrust	$m\,s^{-1}$
T_w	wall temperature	K
v	velocity	$m\,s^{-1}$
z	altitude	m

Acronyms

AR	aspect ratio
ATR	air turbo-rocket
DMR	dual-mode ramjet
HSI	high speed intake

LSI	low speed intake
MR	air-to-fuel ratio
TPR	total pressure recovery

Greek symbols

α_c	intake mass capture ratio	
β	ratio of flow areas	
χ	ratio of mass flows	
η	adiabatic efficiency	
γ	ratio of heat capacities	
μ	viscosity	$kg\,m^{-1}\,s^{-1}$
π	pressure ratio, number π	
ρ	density	$kg\,m^{-3}$
ξ	friction factor	m^{-1}

Sup-/subscripts

0	stagnation quantity
∞	free-stream conditions

Other symbols

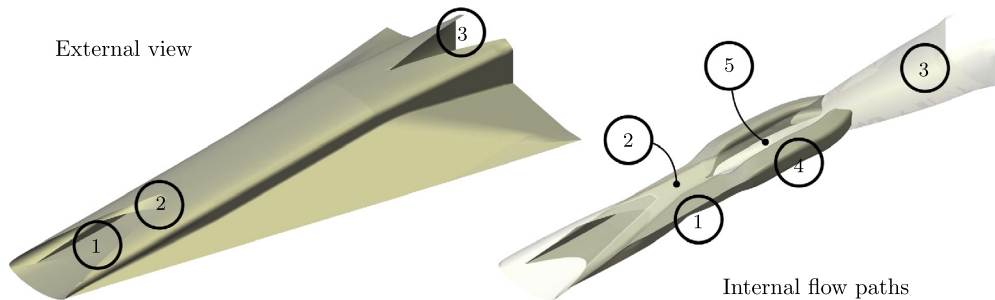|		
$\dot{m}$	mass flow	$kg\,s^{-1}$
$\dot{q}$	heat flux	$kg\,s^{-3}$
$\mathcal{F}$	thrust	$kg\,m\,s^{-2}$
$\mathcal{F}_u$	uninstalled thrust	$kg\,m\,s^{-2}$
$\boldsymbol{u}$	control vector	

Fig. 1. Rendering of the Mach 8 cruise aircraft: **1** low speed intake, **2** high speed intake, **3** nozzle, **4** ATR duct, **5** DMR duct.

air turbo-rocket combustion chamber and the nozzle was computed considering the allocated flow areas along these components. The importance of the airframe-intake integration in the supersonic regime is well known and has been addressed since long time [4], here time-averaged Euler calculations provided the performances of the high and the low speed intakes in the range of flight speeds from Mach 1.5 to 4.5 [23,24].

2. Numerical model

Fig. 3 sketches the flow paths through the aircraft propulsion plant. In the intake, at stations 21 and 20, the inlet air flow is split into two streams to feed the ducts of the air turbo-rocket and the dual-mode ramjet respectively. Hence, in the numerical model, two distinct intakes are considered, together with their respective performance, i.e. mass capture and total pressure recovery: the low speed intake (LSI, stations 10 to 211) and the high speed intake (HSI, stations 10 to 80, i.e. including the ramjet isolator). The exhausts of both engines and the bypassed air flow come together at the entrance of the nozzle (stations 802 and 812).

The low speed intake discharges at the fan inlet plane (station 211). The cross areas at each station are listed in Table 1. The
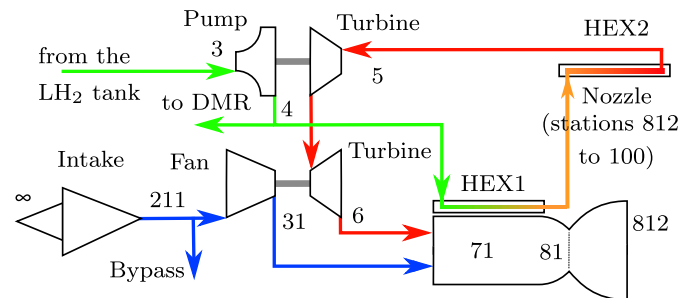

Fig. 2. The air turbo-rocket expander cycle.

total cross section allocated to the air turbo-rocket engines (stations 211 and 31) is 10% larger than the cross section of the throat when fully open (station 81). The inviscid time-averaged Euler calculations in the range of flight Mach numbers 1.5 to 4.5 by Meerts et al. [23,24] yielded the mass capture and total pressure recovery through the low and high speed intakes displayed in Fig. 4, as well as the outlet Mach number and the spillage drag of the high speed intake listed in Table 2. The total pressure recovery across the low speed intake was computed for the most favorable
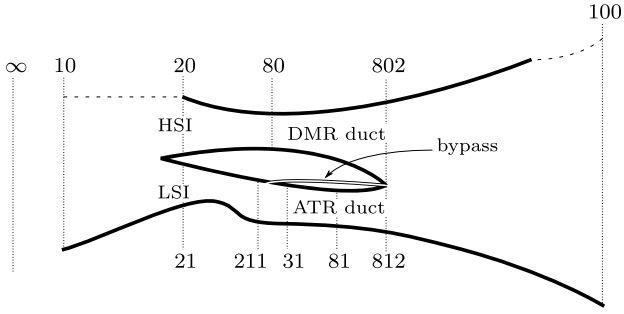
Fig. 3. Station numbering of the combined propulsion plant.

Table 1
Flow areas along the propulsion plant.

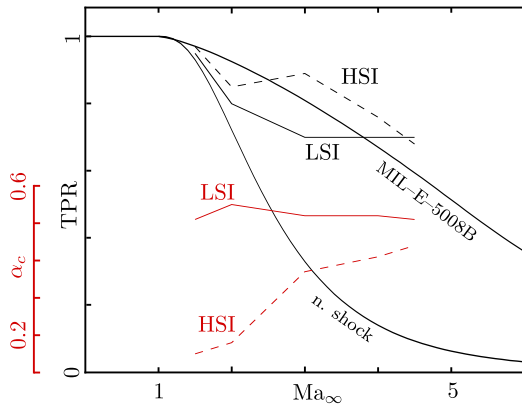| DMR duct		ATR duct	
Station	A [m^2]	Station	A [m^2]
10	37.7		
20	7.3	**21**	10.9
		211	19.1
		31	19.1
80	4.9	**81**	17.4
802	15.9	**812**	20.6
100	111.2		

Fig. 4. Total pressure recovery (TPR) and capture ratio (α_c) vs. flight speed (Ma$_\infty$) [23,24].

case of a normal shock located shortly downstream of the intake throat. Nonetheless, these values were rather conservative when compared to the total pressure recovery across the intake of the supersonic aircraft XB-70, which was simulated at various levels of back pressure [24]. The pressure recovery, mass capture and outlet Mach number from the high speed intake constitute the boundary conditions at station 80. The mass capture ratios of the low and high speed intakes are computed respectively as:

$$\alpha_c^{\text{LSI}} = \dot{m}_{21}/\dot{m}_{10}, \qquad \alpha_c^{\text{HSI}} = \dot{m}_{20}/\dot{m}_{10}$$

Notice that the sum of both quantities is not necessarily unity, as outlined in Fig. 3 some spillage may occur over the intake lip, between stations 10 and 20.

The hydrogen stream within the regenerator is in supercritical state, hence it is described as a real fluid according to the properties database by Lemmon et al. [21]. On the other hand, air is modeled as semi-perfect gas and the combustion gases are designated as a mixture of perfect gases.

Fig. 6 reveals the disposition of the six air turbo-rockets around the dual-mode ramjet. Nevertheless, a single air turbo-rocket is modeled to characterize the flow throughout the six units of the

Table 2
Mach number at the high speed intake exit plane (Ma$_{80}$) and spillage drag coefficient (C_x) [23].

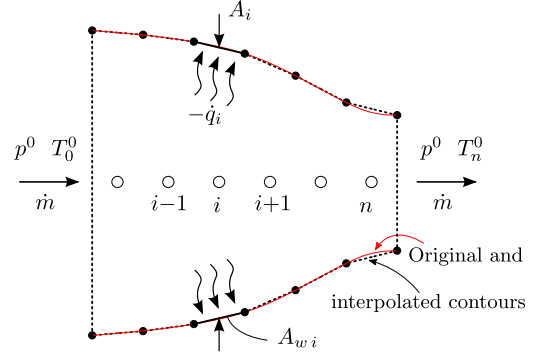| Ma$_\infty$	Ma$_{80}$	C_x
1.5	1.1	0.46
2.0	1.1	0.34
3.0	1.7	0.21
4.0	2.5	0.13
4.5	2.8	0.10

Fig. 5. One-dimensional discretization of the stationary-inviscid fluid flow.

propulsion plant. The dual-mode ramjet (stations 80 to 802) in the center discharges to the nozzle core, and the air turbo-rockets exhaust within the outer annulus of the nozzle.

The air turbo-rocket model is based on the design presented by Rodríguez-Miranda et al. [27]. The fan, pump and turbine are assumed to operate with constant adiabatic efficiencies of respectively 88%, 70% and 60%. The drop of total pressure through the fuel injectors was assumed to be 20% and the drop of total pressure along the fan exhaust and the combustors, including the interaction with the flameholders, was assumed equal to 5%. The combustion chamber and nozzle are comprised between stations 31 and 812. The domain of the air turbo-rocket combustion chamber is discretized in 10 equispaced nodes along the axis (stations 31 to 81) by considering a cylindrical cross area of one sixth the total flow area at station 31.

The flow within the ATR and DMR flow paths, i.e. through stations 80 to 100 and 31 to 100 of Fig. 6, is considered stationary and inviscid. Hence it is described by the equations:

$$\frac{\dot{m}\sqrt{T(h_i^0)}}{p^0 A_i} = \sqrt{\gamma/R_g}\,\text{Ma}_i\left(1 + \frac{\gamma-1}{2}\text{Ma}_i^2\right)^{-\frac{\gamma+1}{2(\gamma-1)}} \tag{1}$$

$$\dot{q}_i A_{wi} = \dot{m}\left(h(T_i^0) - h(T_{i-1}^0)\right) \tag{2}$$

$$\frac{p^0}{p_i} = \left(\frac{T_i^0}{T_i}\right)^{\gamma/(\gamma-1)} \tag{3}$$

$$\frac{T_i^0}{T_i} = \left(1 + \frac{\gamma-1}{2}\text{Ma}_i^2\right) \tag{4}$$

where the stagnation pressure (p^0) and mass flow ($\dot{m}$) are constant along the flow path and, together with the inlet stagnation enthalpy ($h(T_0^0)$), constitute the boundary conditions. The cross and wet areas at the ith grid point are respectively A_i and A_{wi}, in Fig. 5. The flow is assumed adiabatic everywhere except within the walls in contact with the regenerator modules (HEX1–2), where the heat flux ($\dot{q}$) is computed as described in the following Section 2.4.

The flow is assumed frozen throughout the combustion chamber (stations 31 to 81), the dual-mode ramjet (stations 80 to 802)
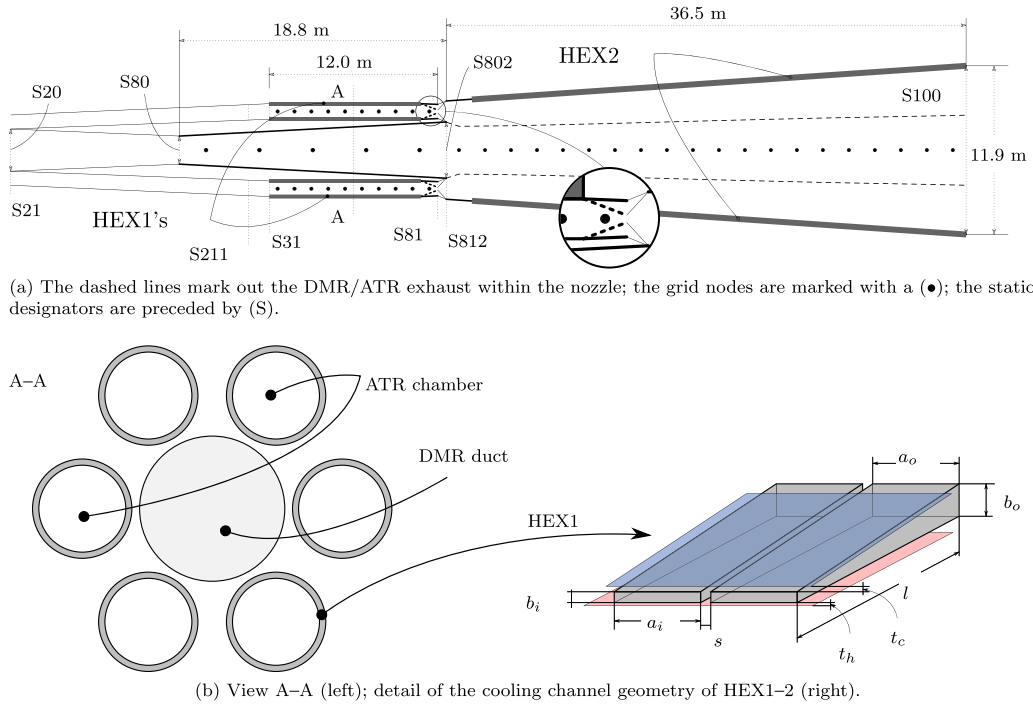
(a) The dashed lines mark out the DMR/ATR exhaust within the nozzle; the grid nodes are marked with a (●); the station designators are preceded by (S).

(b) View A–A (left); detail of the cooling channel geometry of HEX1–2 (right).

Fig. 6. Scaled-down axisymmetric model in EcosimPro.

and the nozzle. The composition of the combustion gases is evaluated in the combustor and the ramjet burner considering a perfect mixture of S species which are described as perfect gases formed among E chemical elements. The molar composition of the mixture ($N_1, N_2, \ldots, N_S$) is the additional unknown which defines the gas thermal and state equations ($\gamma, R_g, h(T), T(h)$) in the system of Eqs. (1) to (4). The gas composition ($\mathbf{N}$) which minimizes the Gibbs potential (G) of the mixture in chemical equilibrium at pressure p and temperature T is:

$$dG = \sum_{k=1}^{S} \frac{\partial G(p, T, \mathbf{N})}{\partial N_k}\bigg|_{p, T, N_{j \neq k}} dN_k = 0 \tag{5}$$

The moles (N_k) of different species (X_k) do not vary independently because mass conservation must be granted, hence the minimization problem is constrained enforcing the total mass (b_j) of each chemical element (j) to remain constant through the chemical reaction:

$$\sum_{\forall k \in R} N_k X_k \rightleftharpoons \sum_{\forall k \in P} N_k X_k$$

$$\sum_{k=1}^{S} a_{jk} N_k = b_j, \quad j = 1 \ldots E \tag{6}$$

In the above expression R and P stand respectively for the set of reactants and products and the mass of atoms j in the species k is denoted as a_{jk}.

The constrained minimization problem defined by Eqs. (5) and (6) is solved following the approach of Gordon and McBride [11], via the Lagrange multipliers method for each pair of values of pressure (p) and temperature (T) at stations 31 and 80. The air is treated as a perfect mixture of nitrogen, oxygen and argon such that, in the combustion with hydrogen, 19 reacting species (H_2O_2, H_2O, H_2, N_2, NH_3, ...) are formed from atomic hydrogen, nitrogen and oxygen.

The flow along the combustion chamber of the air turbo-rocket (station 31 to 81) is resolved with a discretization in 10 nodes

along the combustor axis, whereas the divergent duct of the dual-mode ramjet (station 80 to 802) is based on a 5-node discretization, sketched in Fig. 6(a). In turn, both the core and the annular flows through the nozzle (station 802/812 to 100) are resolved with a 20-node discretization. The model provides a preliminary estimation of the thrust contributed by the dual-mode ramjet and the air turbo-rockets, assuming that both exhausts do not mix within the nozzle. The dual-mode ramjet is operated at partial injection owing to the margin to thermal choke in the throat (station 80) above flight Mach 1.5. This further ensures a smooth transition towards ramjet operation above Mach 4.5. The fan by-pass discharges within the core of the nozzle and mixes with the exhaust from the dual-mode ramjet at station 802. Further considerations on the models of the nozzle, the dual-mode ramjet and the bypass are introduced in the following Sections 2.1 to 2.3. The flow within the axial cooling channels of the regenerator is solved with the one-dimensional form of the unsteady conservation equations. A one-to-one correspondence exists between the nodes of the heat exchanger modules (HEX1's and HEX2) and the nodes of the combustion chamber and nozzle, with the exception of the throat, which is uncooled. Section 2.4 provides additional insight into the model of the regenerator.

The numerical model of the propulsion plant is represented by the system of algebraic-differential equations:

$$\begin{cases} \mathbf{F}(\dot{\mathbf{x}}, \mathbf{x}, t; \mathbf{u}) = 0 \\ \mathbf{x}(t_0) = \mathbf{x}_0 \end{cases} \tag{7}$$

which is integrated with the Differential-Algebraic System Solver algorithm (DASSL) [26] in EcosimPro. The state vector ($\mathbf{x}(t)$) depends on the initial conditions ($\mathbf{x}_0$) and the control vector ($\mathbf{u}(t)$). The stationary solutions of Eq. (7) ($\mathbf{x}_s(\mathbf{u})$) are found at the discrete points $\mathbf{u}^n$ by integrating Eq. (7) from the neighboring solution $\mathbf{x}_s^{n-1}$, corresponding to $\mathbf{u}^{n-1}$ such that:

$$\mathbf{x}_0^n = \mathbf{x}_s^{n-1}$$

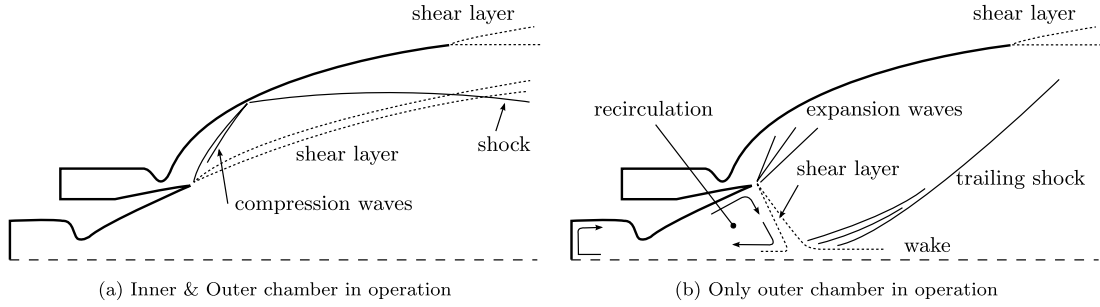$$\mathbf{x}_s^n = \mathbf{x}_s(\mathbf{u}^n), \quad \mathbf{u}^n = \mathbf{u}^{n-1} + \Delta \mathbf{u} \tag{8}$$

(a) Inner & Outer chamber in operation

(b) Only outer chamber in operation

Fig. 7. Flow field in a dual-expander nozzle [12].

The solution $\boldsymbol{x}_s^0$, which is known a priori, corresponds to the starting coordinates $\boldsymbol{u}^0$ in the control space U and the operational envelope E is the subset of the control space U which contains the stationary solutions of Eq. (7):

$$E = \left\{ \boldsymbol{u} \in U : \ \boldsymbol{F}(\boldsymbol{0}, \boldsymbol{x}_s, t; \boldsymbol{u}) = \boldsymbol{0} \ \forall t \right\}$$

As a result, the engine performance $(\mathcal{F}, I_{sp}, T_{sp}, \ldots)$ is a function $\mathcal{P} : E \to \mathbb{R}$ which assigns a scalar to each point of the operational envelope:

$$\mathcal{P}(E) = \left\{ p \in \mathbb{R} : \ p = \mathcal{P}\big(\boldsymbol{x}_s(\boldsymbol{u}), \boldsymbol{u}\big) \right\}$$

The operational envelope is determined assuming that the vector $\Delta \boldsymbol{u}$ is aligned with one of the canonical directions of U, i.e. if $U \in \mathbb{R}^3$ then $\Delta \boldsymbol{u}$ is $(u_1, 0, 0)$, $(0, u_2, 0)$ or $(0, 0, u_3)$.

2.1. Nozzle

The expansion ratio of the dual-expander nozzles is varied operating either the inner or the outer nozzle at high altitude for large expansion ratio, or both for low expansion ratio at lower altitude, outlined in Fig. 7. In alternative designs, the jet angularity and expansion ratio was proposed to be controlled with hinged flaps [14]. The airframe-integrated nozzle was assumed to be of the dual-expander type, where the inner contour is constituted by the nozzle of the dual-mode ramjet, stations 80 to 802 in Fig. 6, whereas the outer contour comprises the divergent section of the air turbo-rocket nozzles (stations 81 to 812) and their prolongation to the exit plane (station 100).

The air turbo-rockets discharge within the outer annulus along the nozzle wall, whereas the dual-mode ramjet exhausts to the nozzle core. The nozzle, which has an area ratio $(A_{100}/(A_{80}+A_{81}))$ of 5, does not run fully during the low speed regime. However, the recirculating zone is assumed to be confined in the core flow. In this manner, by avoiding flow separation from the wall, the surface available for the heat pick-up extends along the complete nozzle wall, where 50% of the heat release to the hydrogen stream takes place. This allows to dispense with a H_2-gas heat exchanger within the air turbo-rocket combustion chamber in favor of the nozzle cooling jacket (HEX2).

The wake is restricted to the nozzle core for a flow configuration expected similar to that of a dual-expander nozzle with the outer chamber in operation, as described in Fig. 7(b). Actually, in the aircraft under consideration, the discharge from the dual-mode ramjet fills the inner chamber and transfers momentum to the wake, hence the outer flow should be even less prone to separation. The simulation of the complex flow field within the nozzle is far from the possibilities of the available one-dimensional model. The flow in the nozzle is considered stationary, diabatic and inviscid, and the gas is treated as ideal and calorically perfect. The resulting system of Eqs. (1) to (4) is solved for each flow stream: core and annulus. The solution consists of a pair of values of each

pressure, temperature and Mach number in the core and the annular flow at discrete locations along the nozzle axis.

The ratio of the cross area for which the fluid vein chokes to the actual flow area: $(A^*/A)_i$, and the Mach number are, in virtue of Eqs. (1), (3) and (4), function of the static to stagnation pressure ratio (p_i/p^0):

$$\left(A^*/A\right)_i = \sqrt{\frac{2}{\gamma - 1}\left(\frac{\gamma + 1}{2}\right)^{\frac{\gamma+1}{2(\gamma-1)}}} \sqrt{\frac{(p^0/p_i)^{\frac{\gamma-1}{\gamma}} - 1}{(p^0/p_i)^{\frac{\gamma+1}{\gamma}}}} \tag{9}$$

$$\mathrm{Ma}_i = \sqrt{\frac{2}{\gamma - 1}\left(\big(p^0/p_i\big)^{\frac{\gamma-1}{\gamma}} - 1\right)} \tag{10}$$

where the stagnation pressure (p^0) equals the combustion pressure of the dual-mode ramjet (p_{802}^0) or the air turbo-rocket (p_{812}^0), in each case of the core or the annular flow. The critical area (A_i^*) results from the evaluation of Eq. (1) at sonic conditions:

$$A_i^* = \frac{\dot{m}\sqrt{T_i^0}}{p^0\sqrt{\gamma/R_g}}\left(\frac{\gamma + 1}{2}\right)^{\frac{\gamma+1}{2(\gamma-1)}}$$

which, if the mass flow is fixed by a sonic throat upstream, indicates that the reduction of stagnation temperature, due to the heat release across the nozzle walls, implies a reduction in the critical area. Furthermore, this decrease of critical area accelerates the flow, as shown by Eqs. (9) and (10) in Fig. 8. Nonetheless, the decrease of sound speed respect to an adiabatic expansion motivates a reduction of thrust.

When an underexpanded jet discharges to the atmosphere, the flow area downstream of the nozzle exit section increases with the difference between the jet and the external pressures. In a first order approximation, the opening of the jet cross-area can be assumed proportional to this pressure jump. For the particular case of the flow within the nozzle, where both annular and core flows coexist, the opening of the annular flow within the nozzle is computed as the ratio of the flow area through the annulus to the nozzle cross area (β_i), and assumed proportional to the difference in static pressures between the annular and the core flows at each axial location:

$$(p_{1i} - p_{0i})/k = \beta_i$$
$$\beta_i = A_{1i}/(A_{0i} + A_{1i}) \tag{11}$$

where A_{1i} and A_{0i} are the flow areas of respectively the annular and the core fluid veins at node i. Eq. (11) can be rewritten as:

$$\frac{A_{81}}{A_{1i}} = \frac{A_{81}}{A_{0i} + A_{1i}}\frac{k}{p^0}\frac{1}{p_{1i}/p^0 - p_{0i}/p^0} \tag{12}$$

where the first term on the right hand side is the ratio of the air turbo-rockets throat to the nozzle flow area at each nodal location,
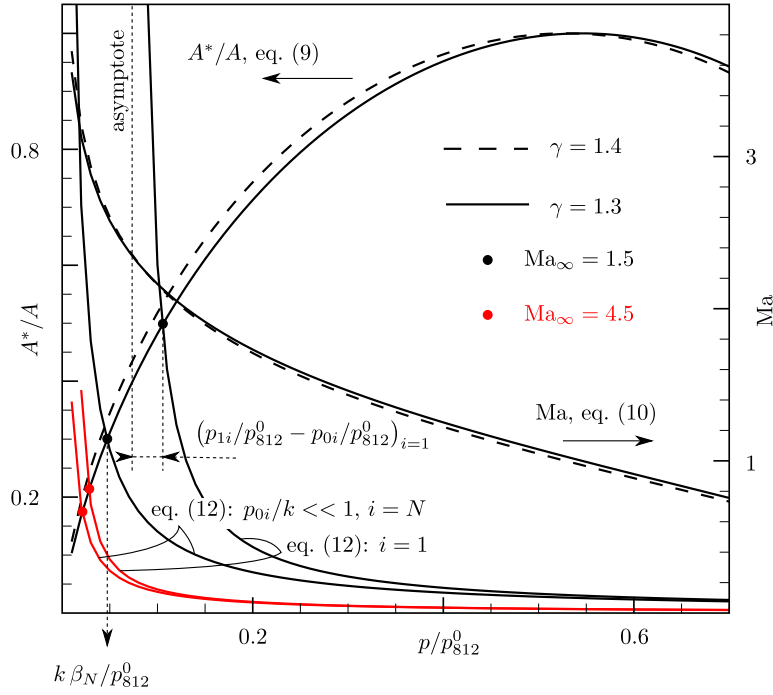
Fig. 8. Cross area and Mach number of the annular flow in function of the expansion ratio (p/p_{812}^0) at $Ma_\infty = 1.5$ and $Ma_\infty = 4.5$.

which is determined by the nozzle profile. The intersection between the curves defined by Eqs. (9) and (12) determines the cross area of the annular vein displayed in Fig. 8. The pressure difference between the central and the annular fluid veins is the distance between the intersection point and the asymptote in Eq. (12), as shown in Fig. 8 for the first node of the discretization $(i = 1)$. The opening of the annular flow is insensitive to the core pressure if $p_{0i}/k \ll 1$, in which case Eq. (11) yields that the pressure in the annulus is solely function of the sensitivity (k): $p_{1i} \sim k\beta_i$. Thus, the pressure ratio within the annular vein at the nozzle exit (p_{1N}/p_{812}^0) is: $k\beta_N/p_{812}^0$, while in nominal conditions at Mach 1.5, in Fig. 8. The corresponding pressure ratios at the nozzle inlet and outlet for nominal conditions at Mach 4.5 are as well shown.

The detachment of the annular flow at low altitudes reduces drastically the heat pick-up from the nozzle wall. This is avoided by selecting a sensitivity which ensures a nozzle exit pressure (p_{1N}) above the assumed separation value: $p_{1N} > 0.3p_\infty$, where N is the number of nodes of the nozzle discretization. The chosen sensitivity in order to avoid detachment while the propulsion plant operates at conditions along the nominal ascent trajectory (see Table 5) is 10 kPa.

2.2. Dual-mode ramjet combustor

The high speed intake operates just above the critical regime; the Mach number at the throat of the dual-mode ramjet (station 80) is slightly supersonic at low Mach numbers ($Ma_\infty < 2.5$) [23]. The throat Mach number increases together with the margin to thermal choke as the flight speed increases. In consequence, the ram burner can be partially operated to compensate the momentum lost through intake and duct and the engine transitions smoothly towards the ramjet operational mode.

The combustion is considered to be adiabatic and takes place downstream of a normal shock wave located at station 80^- with constant stagnation pressure (p^0), Fig. 9 and Eq. (13). The products are in chemical equilibrium and their composition is such that the potential of Gibbs is minimum, Eq. (14). The amount of fuel $(\dot{m}_{H_2})$ required to have sonic conditions at station 80^+ is computed by
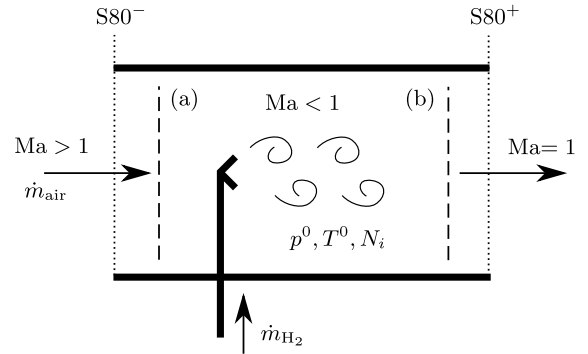

Fig. 9. DMR combustor: normal shock (a) and thermal choke (b).

means of Eq. (15), which is the expression of the mass flow parameter (MFP) for an isentropic evolution along a duct [14].

$$\left(\dot{m}h^0\right)_{air} + \left(\dot{m}h^0\right)_{H_2} = (\dot{m}_{air} + \dot{m}_{H_2})h\left(T^0\right)_{prod} \tag{13}$$

$$dG = \sum_{k=1}^{S} \left.\frac{\partial G(p, T, \boldsymbol{N})}{\partial N_k}\right|_{p^0, T^0, N_{j\neq k}} dN_k = 0 \tag{14}$$

$$\text{MFP} = \frac{(\dot{m}_{air} + \dot{m}_{H_2})\sqrt{T^0}}{p^0 A_{80}} = \sqrt{\gamma/R_g}\left(\frac{\gamma+1}{2}\right)^{-\frac{\gamma+1}{2(\gamma-1)}} \tag{15}$$

For simplicity, the stoichiometry of the combustion as well as the mass conservation equations are not added to the above system of Eqs. (13) to (15), which resolves the fuel flow, the adiabatic combustion temperature (T^0) and the composition of the products $(N_1, \ldots, N_S)$. The combustion gases are represented by the semi-perfect gas model and both the gas constant (R_g) and the ratio of specific heats (γ) are computed from the static temperature corresponding to sonic conditions at station 80^+, whereas the composition is calculated at the stagnation conditions and assumed frozen.

2.3. Air turbo-rocket bypass

The study by Rodríguez-Miranda et al. [27] showed that the uninstalled thrust largely exceeded the mission requirements between flight Mach 1.2 and 2. Consequently, considering that the throat opening was maximum in this regime, the air turbo-rockets were fit with a bypass that allowed reducing the fan compression ratio whereas the thrust contribution by the bypassed flow was disregarded. The bypass allows the intake capacity to match the demand from the air turbo-rockets, such that the air in excess is diverted from the intake to the nozzle. On the other hand, the flow demanded by the air turbo-rockets cannot exceed the mass capture of the intake, which ultimately limits the operation of the propulsion plant.

The bled air is re-injected at the axial location where both the air turbo-rocket and the dual-mode ramjet nozzles join, in Fig. 3. The re-injection upstream of this point would limit the bleeding capacity, as the choke margin within the divergent duct of the dual-mode ramjet is lower. On the contrary, the bypassed air cannot be re-injected downstream of station 802 and along the nozzle centerline without a redesign of the nozzle. The mixing of the bypassed air and the exhaust of the dual-mode ramjet is assumed ideal, i.e. entropy and enthalpy are conserved in the process. The bled air is expanded isentropically to the static pressure of the mixture at station 802. The equilibrium composition of the mixture is not recomputed because the air-to-fuel ratio in the dual-mode combustor is high (typically above 150 with the dual-mode ramjet at partial load). The amount of bypassed air flow is limited by the blockage of the section at station 802 and sets a minimum operational fan compression ratio depending on the opening of the air turbo-rockets throat, as discussed in the following Section 3.

2.4. Regenerator

The air turbo-rocket expander incorporates a heat exchanger between the stream of hot gases from the combustion chamber and the stream of hydrogen that feeds the turbine. A possible design consists in placing the heat exchanger within the combustion chamber, in the flow path of the combustion gases [31]. Nevertheless, the large extension of the wet surfaces of the propulsion plant justifies a design where the heat exchange takes place across the combustion chamber and nozzle walls.

The hydrogen is firstly fed through an array cooling channels mounted on the wall of the air turbo-rocket combustion chamber (HEX1). These heat exchangers, one per air turbo-rocket unit, discharge to the cooling jacket of the nozzle (HEX2), which ultimately feeds the turbine. The flow within the cooling channels of the regenerator is described by the one-dimensional conservation equations of mass, energy and momentum:

$$\frac{\partial \boldsymbol{\omega}}{\partial t} + \frac{\partial \boldsymbol{f}(\boldsymbol{\omega})}{\partial x} = \boldsymbol{\Omega}(\boldsymbol{\omega})$$

which are solved with a centered scheme [9,10]. The conservative variables, flux and source terms are respectively:

$$\boldsymbol{\omega} = A \left\{ \begin{array}{c} \rho \\ \rho v \\ \rho e \end{array} \right\}$$

$$\boldsymbol{f}(\boldsymbol{\omega}) = A \left\{ \begin{array}{c} \rho v \\ \rho v^2 + p \\ \rho v(e + p/\rho) \end{array} \right\}$$

$$\boldsymbol{\Omega}(\boldsymbol{\omega}) = \left\{ \begin{array}{c} 0 \\ -0.5\xi \rho v|v|A/D_h + p(dA/dx) \\ \dot{q} \end{array} \right\}$$

The friction factor is computed from the correlation by Churchill [7], valid for laminar, turbulent and transitional flows:

$$\xi(\mathrm{Re}, \epsilon_r/D_h) = 8\big((8/\mathrm{Re})^{12} + (K_1 + K_2)^{-3/2}\big)^{1/12}$$

$$K_1 = \big[-2.457 \ln\big((7/\mathrm{Re})^{0.9} + 0.27\epsilon_r/D_h\big)\big]^{16}$$

$$K_2 = (37530/\mathrm{Re})^{16}$$

where the absolute rugosity of the channel inner walls (ϵ_r) is assumed of 50 μm. The heat flux ($\dot{q}$) is calculated as

$$\dot{q} = k/D_h(T_w - T)\mathrm{Nu}$$

where the Nusselt number is computed with the correlation by Churchill and Usagi [8], valid in the range $0 < \mathrm{Pr} < \infty$ and $2100 < \mathrm{Re} < 10^6$ of Prandtl and Reynolds numbers:

$$\mathrm{Nu} = \sqrt[10]{\mathrm{Nu}_l^{10} + \left(\frac{\exp(\frac{2200-\mathrm{Re}}{365})}{\mathrm{Nu}_l^2} + \frac{1}{\mathrm{Nu}_t^2}\right)^{-5}}$$

The mean laminar Nusselt number (Nu_l) is: $(\mathrm{Nu}_q + \mathrm{Nu}_T)/2$, where the value for laminar fully developed flow through a tube with constant heat flux across the walls (Nu_q) is 4.364 and, if the temperature of the walls is maintained constant instead of the heat flux, the Nusselt number (Nu_T) is 3.657. The turbulent Nusselt number is computed as:

$$\mathrm{Nu}_t = \mathrm{Nu}_0 + \frac{0.079\sqrt{\xi/2}\,\mathrm{Re}\,\mathrm{Pr}}{(1 + \mathrm{Pr}^{4/5})^{5/6}}$$

where the constant contribution (Nu_0) corresponds to the averaged value: $(\mathrm{Nu}_{0q} + \mathrm{Nu}_{0T})/2$, being 4.8 and 6.3 the Nusselt numbers for respectively constant wall temperature and heat flux. The Reynolds and Prandtl numbers are based on the bulk properties of the fluid and the hydraulic diameter (D_h).

Regarding the heat flux to the hot side of the wall, the steady one-dimensional conservation Eqs. (1) to (4) resolve the inviscid and diabatic flow along the combustion chamber and nozzle. The nozzle core-flow is considered adiabatic, thus the heat flux ($\dot{q}_i$) is null, in Eq. (2). As for the flow within the combustion chamber and the nozzle annulus, the heat to the gases comprises a convective and a radiative term:

$$\dot{q}_i = h_{ci}(T_{wi} - T_{ai}) - \dot{q}_{ri}$$

where the adiabatic wall temperature (T_{ai}) is defined as:

$$T_{ai} = T_i\big(1 + 0.5\mathrm{Pr}_i^{1/3}(\gamma_i - 1)\mathrm{Ma}_i^2\big)$$

and the heat transfer coefficient (h_c) is computed from the correlation proposed by Bartz [2]:

$$h_{ci} = 0.026\mu_i^{0.2}(k_i/\mu_i)^{0.6}C_{pi}^{0.4}\dot{m}^{0.8}/A_i^{0.9}(0.25\pi D_{th}/R_c)^{0.1}$$

The thermal and transport properties of the combustion gases (Pr_i, γ_i, C_{pi}, μ_i and k_i) are evaluated at the temperature: $0.5(T_{wi} + T_i)$, halfway between the bulk and the wall temperatures. The throat diameter and curvature radius are respectively D_{th} and R_c. The convective heat transfer to the nozzle wall decreases significantly in case of flow separation, thus the heat transfer coefficient is reduced by 90% at the locations (i) where, according to the criterion of Summerfield [22], the pressure reaches 30% of the ambient pressure.

The radiation in the combustion chamber and nozzle is mainly due to the presence of soot, carbon dioxide and water vapor. Nonetheless, the content of carbon dioxide in atmospheric air is very low (<0.4‰ vol.) and the presence of soot is meaningful only if hydrocarbon fuels are utilized. Hence, the radiative heat flux in the combustion of air with hydrogen is solely due to the presence of the water vapor and is computed from the following expression reported by Barrére et al. [1]:

Table 3
Regenerator design space.

	D_{hi} [mm]	AR_i	AR_o
HEX1	[0.5, 50]	[0.05, 10]	[0.05, 50]
HEX2	[1, 50]	[0.05, 10]	[0.05, 50]

$$\dot{q}_{ri} = 4.07 \left(p_i^{H_2O}\right)^{0.8} L_i^{0.6} \left(\left(\frac{T_i}{100}\right)^3 - \left(\frac{T_{wi}}{100}\right)^3\right)$$

which is function of the partial pressure of water in the combustion gases (p^{H_2O}), the bulk temperature of the combustion gases (T) and the temperature of the combustor or nozzle walls (T_w). The directional average of the thickness of the medium, as seen from a point on the chamber or nozzle surface, is the mean length of the beam (L) which, assuming an infinite cylinder of diameter D radiating to the surface, is approximated by $L \sim 0.9D$ [3]. The so computed radiation by water vapor is typically 6% of the total heat transferred to the chamber walls and even lower in the nozzle.

There are a total of 6 regenerator units (HEX1) located around the combustion chamber wall, each one is composed of a number (N_{ch}) of straight cooling channels disposed around each of the air turbo-rocket chambers, Fig. 6. The channels of the cooling jacket (HEX2) are disposed around the nozzle wall, in Fig. 6(a). Both HEX1 and HEX2 modules are arranged in co-flow with the hot gases and their geometry is determined by the widths ($a_{i/o}$) and heights ($b_{i/o}$) of the channel inlet ($_i$) and outlet ($_o$), the channel length (l), the thickness of the wall in contact with the hot gases (t_h), the thickness of the outer wall (t_c) and the thickness of the wall between the channels (s), in Fig. 6(b) (right).

The outer walls are assumed adiabatic, hence the thicknesses (t_c) do not affect the performance of the regenerator. In turn, the hot wall hinders the heat transfer phenomena and should be as thermally thin as possible. Values of the wall thickness of few tens of millimeter are common practice in rocket engineering [9, 18,30]. A hot wall thickness (t_h) of 0.3 mm and a conservative low value of the thermal conductivity, which corresponds to titanium, were considered for the channel walls of both modules. The spacing between the cooling channels (s) is 1 mm, constant along the HEX1 and HEX2 channels, which have a length (l) of respectively 10.8 m and 34.7 m. Regarding the nozzle module (HEX2), the channel width varies to accommodate the diameter change for a constant channel spacing along the nozzle. The remaining parameters which determine the geometry of the cooling channels are the hydraulic diameter at the inlet (D_{hi}) and the aspect ratios at the inlet (AR_i) and outlet (AR_o), which are computed as:

$$AR = b/a, \qquad D_h = 2ab/(a + b)$$

The heat transfer performance of the regenerator is traded off by the pressure loss along the channels: a suitable thermal performance can be achieved by increasing the surface in contact with the hydrogen in detriment of the pressure drop. Nonetheless, the power consumed by the hydrogen pump is considerably outbalanced by the fan power, which is two orders of magnitude larger. In consequence, the energetic cost of compensating the larger pressure losses of a regenerator with improved thermal performance is much lower than the losses incurred by over expansion through the turbine in case of insufficient heat pick-up. Hence, the design of the regenerator is driven by the minimization of the turbine expansion ratio. The optimum design was determined by means of the optimization routine by Verstraete [33], which is based on a differential evolution algorithm. Table 3 defines the bounds of the regenerator design space.

The optimization was performed considering a chamber pressure of 106 kPa while on flight at Mach 1.5, conditions for which

Table 4
Optimum cooling channel geometry.

		D_h [mm]	AR	a [mm]	b [mm]	N_{ch}
HEX1	in	6	0.05	66	3	94
	out	10	0.08	66	5	
HEX2	in	19	0.09	114	10	198
	out	18	0.05	188	9	

the uninstalled thrust of the air turbo-rockets fulfills the installed thrust required by the mission. The minimum turbine expansion ratio was found to be 18.5 and the overall heat pick-up was 480 MW, which supports the conservative estimation of 390 MW by Rodríguez-Miranda et al. [27]. Nonetheless, the chamber pressure had to be raised to compensate the spillage drag of the high speed intake, which led to a turbine expansion ratio of 30, as reported in the following Section 3.

The geometry of each one of the six HEX1 units and the single cooling jacket HEX2 consists of channels of very low aspect ratio, which maximize the exposure of the fluid to the hot wall, in Table 4. In fact, both optimum aspect ratios at the inlet and at the outlet of the regenerator reach the lower bound of the design space. This constitutes an expected result because the heat transfer performance primes over the pressure losses, as discussed previously.

Lightweight high-temperature carbon matrix composites are being considered to manufacture the cooling channels of the regenerator along the combustion chamber and nozzle [13]. Although the lifetime of the proposed channel geometries is under evaluation [6], successful tests of a rocket combustion chamber have been reported [17].

3. Installed performance

The installed performances of the propulsion plant, namely installed thrust ($\mathcal{F}$), specific impulse (I_{sp}) and specific thrust (T_{sp}), are computed as:

$$\mathcal{F} = \mathcal{F}_u^{ATR's} + \mathcal{F}_u^{DMR} - 1/2\left(\rho v^2\right)_\infty C_x A_{10}$$

$$I_{sp} = \frac{\mathcal{F}}{\dot{m}_{H_2}^{ATR's} + \dot{m}_{H_2}^{DMR}} \tag{16}$$

$$T_{sp} = \frac{\mathcal{F}}{(\rho v)_\infty A_{10}(\alpha_c^{HSI} + \alpha_c^{LSI})} \tag{17}$$

where C_x is the coefficient of drag induced by intake spillage and α_c is the mass capture of the low (LSI) or the high speed intake (HSI) presented in Fig. 4. The uninstalled thrust ($\mathcal{F}_u$) of the air turbo-rockets (ATR's) and the dual-mode ramjet (DMR) is computed as:

$$\mathcal{F}_u = (\dot{m}v)_s + (p_s - p_\infty)A_s - \left(\rho v^2\right)_\infty A_{10}\alpha_c$$

The fluid veins of each exhaust from the dual-mode ramjet and the air turbo-rockets are computed along the nozzle as explained in Section 2.1. The axial location where the flow through the corresponding fluid vein reaches the base pressure is designated as ($_s$) in the previous expression. If the base pressure is not reached, then ($_s$) refers to the conditions within the fluid vein at the nozzle exit (station 100). According to the criterion of Summerfield [22], the base pressure is assumed to be 30% of the ambient pressure (p_∞). Combining Eqs. (16) and (17) and after some algebraic manipulation, the installed specific thrust (T_{sp}) can be expressed in function of the installed specific impulse as:

$$T_{sp} = \frac{1 - B}{(1 - \chi)(1 + \alpha_c^{HSI}/\alpha_c^{LSI})} \frac{I_{sp}}{MR} \tag{18}$$

Table 5
Nominal cycle along the vehicle ascent trajectory.

Flight Mach number, Ma_∞	1.5	2.0	3.0	4.0	4.5
Flight altitude, z [km]	15.8	18.3	21.6	24.3	25.9
Chamber pressure, p_{71}^0 [kPa]	112	109	137	329	429
Chamber mixture ratio, MR	32	32	32	67	65
ATR's total throat area, A_{81} [m^2]	17.37	17.37	13.00	4.00	2.75
LSI capture area, α_c^{LSI} [%]	51	55	52	52	51
HSI capture area, α_c^{HSI} [%]	15	18	37	41	44
LSI total pressure recovery, TPR [%]	95	80	70	70	70
HSI total pressure recovery, TPR [%]	97	85	89	76	68
Fan adiabatic efficiency, η_f [%]			88		
Turbine adiabatic efficiency, η_t [%]			60		
Pump adiabatic efficiency, η_p [%]			70		
Overall consumption, $\dot{m}_{H_2}$ [kg/s]	41.6	40.2	38.2	19.9	18.8
DMR consumption, χ [%]	0.1	0.1	3.5	21.5	26.4
LSI air mass flow rate, $\dot{m}_{21}$ [kg/s]	1461	1407	1185	1049	902
HSI air mass flow rate, $\dot{m}_{20}$ [kg/s]	419	473	847	840	770
LSI bleeding, B [%]	8.9	8.7	0.4	0.2	0.1
Fan compression ratio, π_f	3.2	2.6	1.3	1.1	1.0
Pump pressure ratio, π_p	16	12	7	5	4
Turbine expansion ratio, π_t	30	22	2	3	1
Regenerator pressure loss [%]	14	22	83	31	53
HEX1 pressure loss [%]	7	10	28	13	20
HEX2 pressure loss [%]	8	13	77	21	42
Regenerator inlet pressure, p_4^0 [bar]	47	37	22	15	11
HEX1 maximum wall temperature [K]	570	540	570	700	710
HEX2 maximum wall temperature [K]	880	900	970	1290	1440
Turbine inlet temperature, T_5^0 [K]	840	870	940	1270	1420
Chamber temperature, T_{71}^0 [K]	2290	2310	2480	2110	2270
Heat pick-up ($6 \times$ HEX1 + HEX2) [MW]	491	488	504	284	284
HEX2 heat pick-up [%]	47	47	49	51	52
Turbine power per ATR engine [MW]	31.7	29.7	10.9	6.9	0.3
Fan power [%]	98	98	97	98	56
Pump power [%]	2	2	3	2	44
ATR FV length to base pressure [%][a]	100	100	100	100	100
DMR FV length to base pressure [%][a]	25	40	65	80	95
ATR's thrust, $\mathcal{F}_u^{\text{ATR's}}$ [kN]	1758	1686	1522	842	710
DMR thrust, $\mathcal{F}_u^{\text{DMR}}$ [kN]	2	16	47	160	163
Intake spillage drag [kN]	292	261	215	156	115
Overall installed thrust, $\mathcal{F}$ [kN]	1468	1442	1353	846	759
Installed specific impulse, I_{sp} [km/s]	35	36	35	43	40
Installed specific thrust, T_{sp} [km/s]	0.8	0.8	0.7	0.4	0.5

[a] Length along the ATR/DMR exhaust fluid vein (FV) within the nozzle to reach the base pressure of 0.3 p_∞, according to Summerfield's criterion.

where B is the bleeding ratio, χ is the ratio of fuel mass flow to the dual model ramjet over the global fuel consumption and MR is the mixture ratio in the air turbo-rocket chambers:

$$B = \frac{\dot{m}_{\text{bypass}}}{(\rho v)_\infty A_{10} \alpha_c^{LSI}}$$

$$\chi = \dot{m}_{H_2}^{\text{DMR}} / \left(\dot{m}_{H_2}^{\text{ATR's}} + \dot{m}_{H_2}^{\text{DMR}} \right)$$

$$\text{MR} = \rho_\infty v_\infty A_{10} (1 - B) \alpha_c^{LSI} / \dot{m}_{H_2}^{\text{ATR's}} \qquad (19)$$

Table 5 shows the engine performances at Mach numbers 1.5, 2, 3, 4 and 4.5. The throat opening schedule of the air turbo-rockets obtained by Rodríguez-Miranda et al. [27] in function of the flight Mach number is considered in the current simulation. The opening reaches the maximum space allocated by engine bays below flight Mach 2, thus the chamber pressure is raised for the installed thrust of the propulsion plant to comply with the mission requirements. The rise of chamber pressure reduces the bleeding below 9% and raises the fan compression ratio up to 3.2, as compared to the respective values of up to 22% and 3.0 corresponding to the uninstalled performance calculations [27]. Above Mach 2, the fan compression ratio decreases below a readily achievable value of 2.9 [16] and the optimum throat scheduling can be recomputed once the off-design characteristics of the fan are known.

The heat recovery of about 500 MW for stoichiometric operation from Mach 1.5 to 2.0 constitutes a 25% rise over the estimate in the uninstalled performance calculation. This increase comes together with a rise of air mass flow such that the specific heat pick-up of 380 kJ per kilogram of air into the chamber does not represent more than a 9% increase over the uninstalled calculations. As a consequence, the temperature rise through the regenerator, hence the turbine entry temperature (T_5^0) does not vary appreciably whereas the turbine specific power increases 26% up to 4.4 MJ/kg at Mach 2. This motivates the large turbine expansion ratios required in the range of Mach numbers from 1.5 to 2.0. On the other hand, the turbine power and the fuel consumption decay above Mach 3 and the turbine inlet temperature reaches 1400 K at Mach 4.5.

In the air turbo-rocket the turbine power is delivered independently from the fan performance [5,27]. This feature allows designing the turbine for the most demanding condition, such that the engine can be throttled throughout the flight envelope varying the turbine expansion ratio. As a consequence, the sensitivity of the air turbo-rocket to the recovery pressure of the low speed intake relies on the possibility of operating the fan, pump and turbine at the required compression/expansion ratios and efficiencies. Table 5 shows that the operation of the turbomachinery becomes critical at Mach 1.5, regime at which the fan compression ratio and
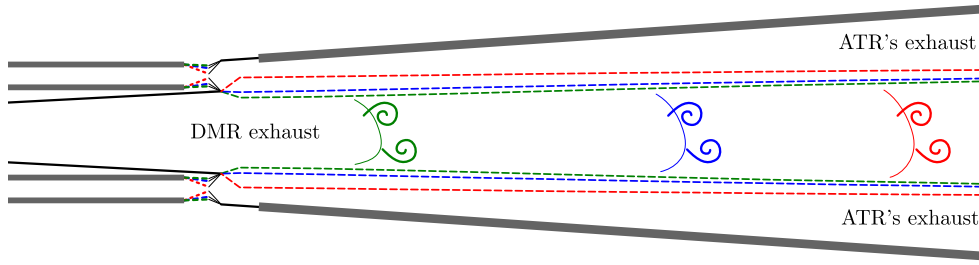
Fig. 10. Opening of the air turbo-rockets throat, flow area of the DMR exhaust within the nozzle core and section where the base pressure ($0.3p_\infty$) is reached for $\text{Ma}_\infty = 1.5$, 3.0 and 4.5.

Table 6
Sensitivity of the turbomachinery to a 5% decrease of total pressure recovery across the low speed intake at flight Mach number 1.5 and 2.

Ma_∞	Fan		Turbine		Pump	
	π_f	$\Delta\pi_f$ [%]	π_t	$\Delta\pi_t$ [%]	π_p	$\Delta\pi_p$ [%]
1.5	3.3	3%	38	27%	19	19%
2.0	2.7	4%	29	32%	15	25%

the turbine expansion ratio are maximum. The eventual decrease of total recovery pressure can be compensated by an equivalent increase of the fan compression ratio in order to hold constant chamber pressure and thrust. Hence, if the pressure recovery drops 5% below the calculated value in Fig. 4, then the fan compression ratio and the turbine expansion ratio should be raised to respectively 3.3 and 38 for flight at Mach 1.5; for flight at Mach 2 and considering a decrease of pressure recovery of the same amount, the fan compression ratio and the turbine expansion ratio should be raised to respectively 2.7 and 29. Thus, the design of both turbine and pump is very sensitive to the intake pressure recovery in the low range of flight speeds, in Table 6.

In the range of flight Mach numbers from 1.5 to 2.0, the transfer of momentum to the high speed stream with the re-injection of the bled air generates positive thrust. The margin to thermal choke at the throat of the dual-mode ramjet increases with the flight Mach number, which allows starting the transition towards ramjet mode by progressively rising the fuel injection to the dual-mode ramjet (χ). At Mach 4 over 20% of the fuel is diverted towards the dual-mode ramjet and the uninstalled thrust of the air turbo-rockets duct alone cancels the intake spillage drag.

Fig. 10 shows a scaled outline of the throat opening and the flow area occupied by the high speed exhaust within the nozzle core at flight Mach numbers 1.5, 3.0 and 4.5. The exhaust of the air turbo-rockets flows within the outer annulus and does not separate from the nozzle wall; the static pressure remains above the limit of $0.3p_\infty$, considered as base pressure. On the contrary, the core flow reaches the base pressure at 25, 65 and 95% of the nozzle length for increasing flight Mach numbers. The dual-mode ramjet and the air turbo-rockets are both in operation at flight Mach number 4.5 and the nozzle is close to run full.

During flight at Mach number 4.5 and altitude of 26 km, the ram compression suffices to achieve a chamber pressure (p^0_{71}) of 429 kPa and the fan power is brought down for a compression ratio (π_f) of 1.0. Fig. 11 presents the installed thrust, specific impulse and bleeding ratio in function of the throat area and mixture ratio of the air turbo-rockets for unitary compression ratio across the fan. The installed specific impulse is maximum along the line of null bleeding ($B = 0$), which therefore defines the optimal engine throttling line at this flight regime. The specific impulse decreases as the bleeding is increased, in the region $B > 0$, whereas the flow demand of the air turbo-rockets exceeds the capacity of the intake in the region of forbidden operation, above the line $B = 0$. The throat area of the air turbo-rockets is set to 2.75 m^2 in
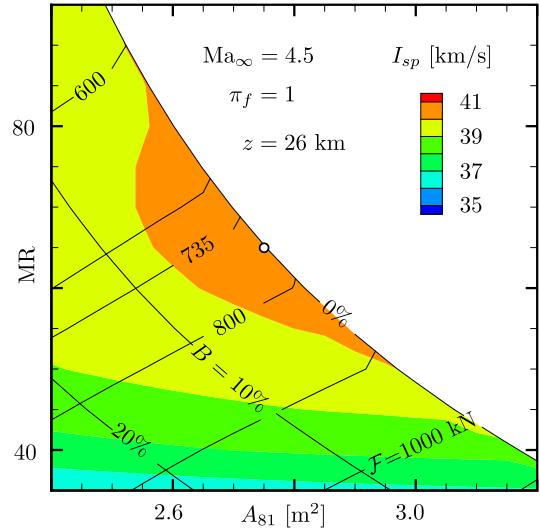

Fig. 11. Installed specific impulse (I_{sp}) and thrust ($\mathcal{F}$), and bleed ratio (B) vs. throat area (A_{81}) and mixture ratio (MR); ($\circ$) indicates the design point.

order to accommodate the intake mass capture, i.e. avoiding bleeding, while the installed thrust is maintained above the value of 735 kN required by the aircraft mission. These settings, for which the installed specific thrust is maximum, define the on-design conditions at Mach 4.5, in Table 5.

4. Operational envelope

Whereas in the previous section the installed performances were obtained along the vehicle ascent trajectory, the flight speed (Ma_∞) and altitude (z) are now varied independently and, together with the chamber pressure (p^0_{71}), the mixture ratio (MR) and the opening of the throat of the air turbo-rockets (A_{th}), define the control vector ($\boldsymbol{u}$) of the system:

$$\boldsymbol{u} = \left(\text{Ma}_\infty, \text{MR}, z, p^0_{71}, A_{81}\right)$$

As opposed to the turbojet, in the air turbo-rocket the turbine can be throttled independently of the mixture ratio, therefore the chamber total pressure (p^0_{71}), or equivalently the fan compression ratio (π_f), constitutes an additional control variable. The mixture ratio (MR) is defined as the ratio of air-to-fuel mass flow in the air turbo-rockets, Eq. (19), whereas the overall mixture ratio of the engine (MR$_o$) accounts as well for the air and fuel flows in the dual-mode ramjet, which depend solely on the flight regime (Ma_∞, z).

The performance database was obtained in two steps. The control space was sampled first for each flight regime $u_1 = \{1.5, 2.0, 3.0, 4.0, 4.5\}$ at discrete points along the $\boldsymbol{u}_2$-direction, which corresponds to the mixture ratio (MR). In this step, the initial conditions ($\boldsymbol{x}^0_s$) of Eq. (8) correspond to the operating points
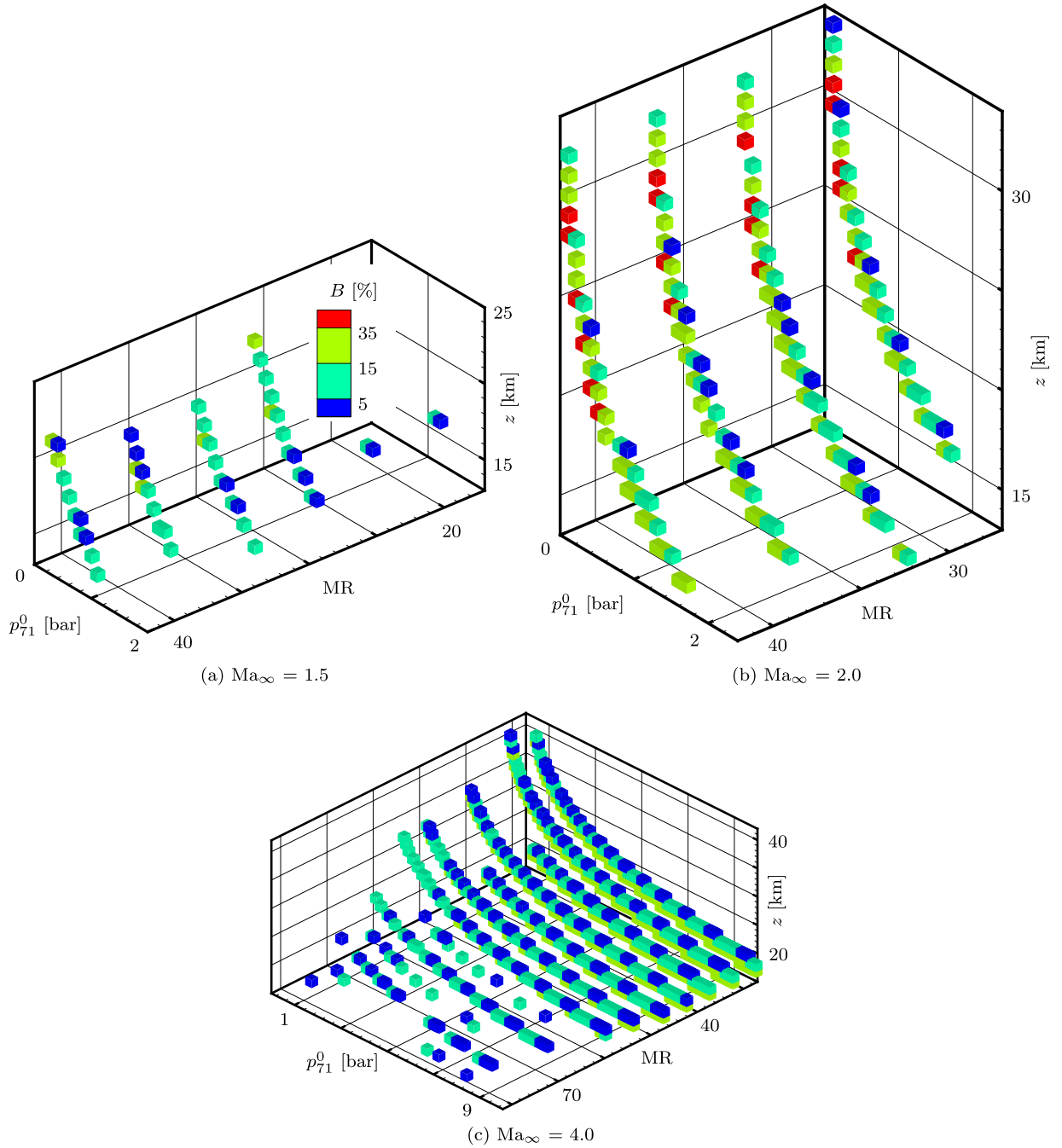
Fig. 12. Operational envelope: low speed intake bleeding (B) at flight Mach numbers 1.5, 2 and 4.

at Mach 1.5, 2, 3, 4 and 4.5 in Table 5, and the values along the $\boldsymbol{u}_2$-direction are limited at very rich mixtures (lower limit) and excessive turbine expansion ratios (upper limit). Secondly, starting from the solutions throughout the plane $(\boldsymbol{u}_1, \boldsymbol{u}_2)$ obtained previously, the control space is traversed within a subspace $\boldsymbol{u}_\perp$ orthogonal to $\boldsymbol{u}_1$ and $\boldsymbol{u}_2$. The subspace $\boldsymbol{u}_\perp$ is coincident with the $\boldsymbol{u}_3\boldsymbol{u}_4$-plane in the cases of $u_1 = \{1.5, 2.0, 3.0, 4.0\}$ and with the $\boldsymbol{u}_3\boldsymbol{u}_5$-plane in case of Mach 4.5. The control space was sampled at regular intervals in altitude, chamber pressure, mixture ratio and throat area to compute the operational envelope which, despite of the discrete representation in Fig. 12, is a connected space. Different step sizes were utilized for each flight speed, in Table 7, nonetheless the results in Fig. 12 are all represented with the same precision.

The engine is modeled as an adiabatic system, thus the thrust performances ($\mathcal{F}, I_{sp}, T_{sp}$) do not depend on the regenerator heat

Table 7
Step size of the control space sampling.

Ma$_\infty$ (u_1)	Δu_3 [km]	Δu_4 [kPa]	Δu_2 [-]	Δu_5 [dm^2]
1.5	1.0	10	5	n/a
2.0	0.5	5	5	n/a
3.0	0.5	5	5	n/a
4.0	1.0	5	5	n/a
4.5	1.0	n/a	5	10

recovery or the turbomachinery adiabatic efficiency and, in consequence, the throat opening was determined in order to minimize the power demand to the turbomachinery [27]. This scheduling of the throat in function of the flight speed is adopted for the calculation of the operational envelope; further optimization of the throat opening law requires the off-design characterization of the
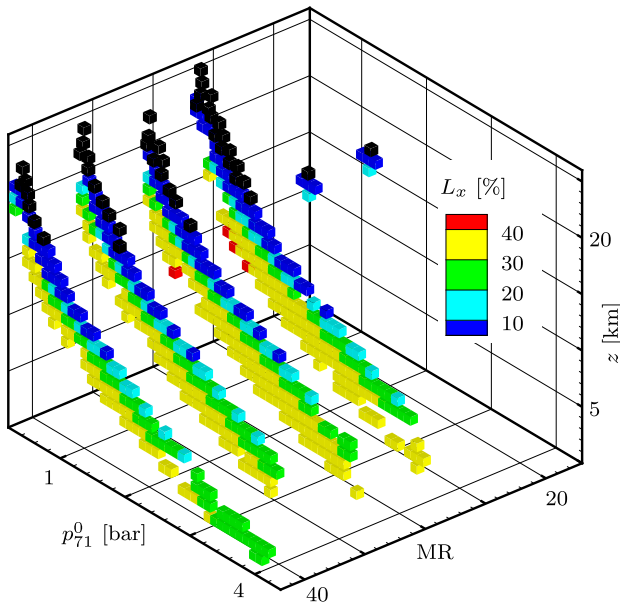
Fig. 13. Feasible nozzle re-injection location (L_x) at $Ma_\infty = 1.5$.

turbomachinery. As a result, the number of control variables for the calculation of the envelopes at flight Mach numbers 1.5, 2.0, 3.0 and 4.0 is reduced to four: Ma_∞, MR, z, p_{71}^0. Regarding the envelope at flight Mach number 4.5, the air turbo-rockets satisfy the thrust requirement while in ramjet operation ($\pi_f = 1$), consequently the chamber pressure is set by the flight regime and is not a control parameter. Thus, the overall throat area of the air turbo-rockets (u_5) is varied instead of the chamber stagnation pressure (u_4).

The bled air from the low speed intake is re-injected within the dual-mode ramjet at station 802. The flow capacity at this station determines the amount of bleeding and largely reduces the operational envelope. Nonetheless, if the re-injection point is moved downstream of 802, where the nozzle flow capacity is larger, then the bleeding can be increased. Fig. 13 shows the hypothetical re-injection location for an extended operational envelope towards lower altitudes. This distance (L_x) is referred to station 802, corresponding to the grid node within the first 10% of the nozzle, thus values $L_x > 10\%$ indicate re-injection downstream of 802. Nevertheless as explained in Section 2.3, a re-injection downstream of 802 requires the redesign of the nozzle contour, thus this operational region cannot be reached. On the other hand, the air turbo-rockets require an air flow rate in excess of the intake mass capture at high altitudes, therefore these operational points, colored in black in Fig. 13, are unreachable. Upon these considerations, the operational envelope is limited to the region shown in Fig. 12(a). Above flight Mach 1.5, the re-injection at station 802 does not restrict the operational range, which is largely increased, in Figs. 12(b) and 12(c). This gain comes at the cost of bleeding up to 35% of the flow to the air turbo-rockets duct at Mach 2: since the thrust requirement is maximum in the low speed regime ($Ma_\infty \leqslant 2.0$), the throats of the air turbo-rockets are fully open and cannot be further increased to limit the bleeding.

Fig. 14 displays the installed thrust and specific impulse, the fan compression ratio and the turbine expansion ratio throughout the feasible operational envelope at flight Mach number 1.5. The results indicate that, with the exception of few sparse overlapping points, the operational envelope practically reduces to a surface in the p_{71}^0MRz-space, i.e. the engine lost one degree of freedom. The chamber pressure and mixture ratio depend on each other at low altitudes, as indicated by the shadowed regions in Fig. 14(a). The engine throttlability decreases at increasing flight altitudes:

above 17 km the flight altitude sets the thrust level which, insensitive to the mixture ratio (MR), is governed by the chamber pressure (p_{71}^0), in Fig. 14(a). The points with maximum specific impulse shape the optimal operational envelope, contoured with dotted lines in Fig. 14. In this range, the fan operates at high compression ratios between 3.1 and 3.4, with a peak above 3.4 at low altitude in the vicinity of the design point, in Fig. 14(c). The expansion ratio across the hydrogen turbine is in excess of 30 all over the optimal points and below 19 km of altitude, in Fig. 14(d). The expansion ratio can be substantially lowered by operating the air turbo-rockets at suboptimal conditions, with a lower mixture ratio, or by improving the heat transfer performance of the regenerator.

Fig. 15 shows a continuous representation of the previous results for Mach 1.5 in Fig. 14 obtained by linear interpolation of the data. The operation at each flight altitude is limited for low chamber pressures by the amount of bypassed air, which exceeds the nozzle flow capacity at the re-injection point, whereas the turbine expansion and the fan compression ratios are critical for high chamber pressures, in Fig. 15(a). The operation with low mixture ratios is at the cost of low specific impulse, thus it is not efficient. On the contrary, the heat pick-up, hence the turbine expansion ratio, are compromised for high mixture ratios, i.e. lean combustion. The choking of the section at the re-injection point prevents the flight below 13 km of altitude; the air flow demand of the air turbo-rockets equals the capacity of the low speed intake and sets the upper limit of 19 km.

Fig. 16(a) shows the installed thrust and specific impulse during flight at Mach 2. The decrease of thrust in one third as the flight altitude rises from 15 km to 22 km is solely motivated by the decay of the ambient air density. This is evidenced in Fig. 16(b), where the propulsive system performs with constant installed specific impulse between 25 and 40 km/s and constant specific thrust between 0.4 and 0.8 km/s in the range of flight altitudes considered. In fact, combining Eqs. (17) and (18), the installed thrust can be expressed as:

$$\mathcal{F} = \underbrace{(\rho a)_\infty}_{f(z)} \underbrace{\frac{\alpha_c^{\mathrm{LSI}} Ma_\infty}{(1-\chi)}}_{f(Ma_\infty)} \frac{A_{10}(1-B)}{\mathrm{MR}} I_{sp}$$

which shows that for a given operating point (constant MR, B, I_{sp}) the installed thrust is proportional to $(\rho a)_\infty$ through a term that only depends on the flight Mach number.[1] Moreover, the sensitivity of the thrust to the specific impulse at constant mixture ratio, i.e. the inclination of the MR-lines, is inversely proportional to the altitude by means of $f(z)$. The chamber pressure sets the thrust level, therefore the engine is throttled acting on the fan compression ratio while the mixture ratio is set to maximize the specific impulse. However, the mixture ratio is compromised at low altitudes by an excessive expansion ratio through the turbine, in Fig. 16(a).

The increase of ram compression with the flight Mach number allows to diminish the fan compression ratio. Consequently, the turbine expansion ratio is maintained below 5 for flight speeds above Mach 3. The bleeding at the fan inlet allows to match the air demand from the turbo-rockets to the air flow capture of the low speed intake as the fan compression ratio varies. Hence, the engine is throttled with the chamber pressure by allowing more or less air bleeding. Additionally in Fig. 17(a), the air turbo-rockets, when operated in ramjet mode ($\pi_f \sim 1$) for rich mixtures (MR < 34), exhibit a very high specific impulse, in excess of 40 km/s.

---

[1] In fact, when the altitude rises from 15 to 22 km the air density decreases more than 66% whereas the speed of sound increases less than 1%, therefore the variation of thrust is mostly driven by the free-stream density.
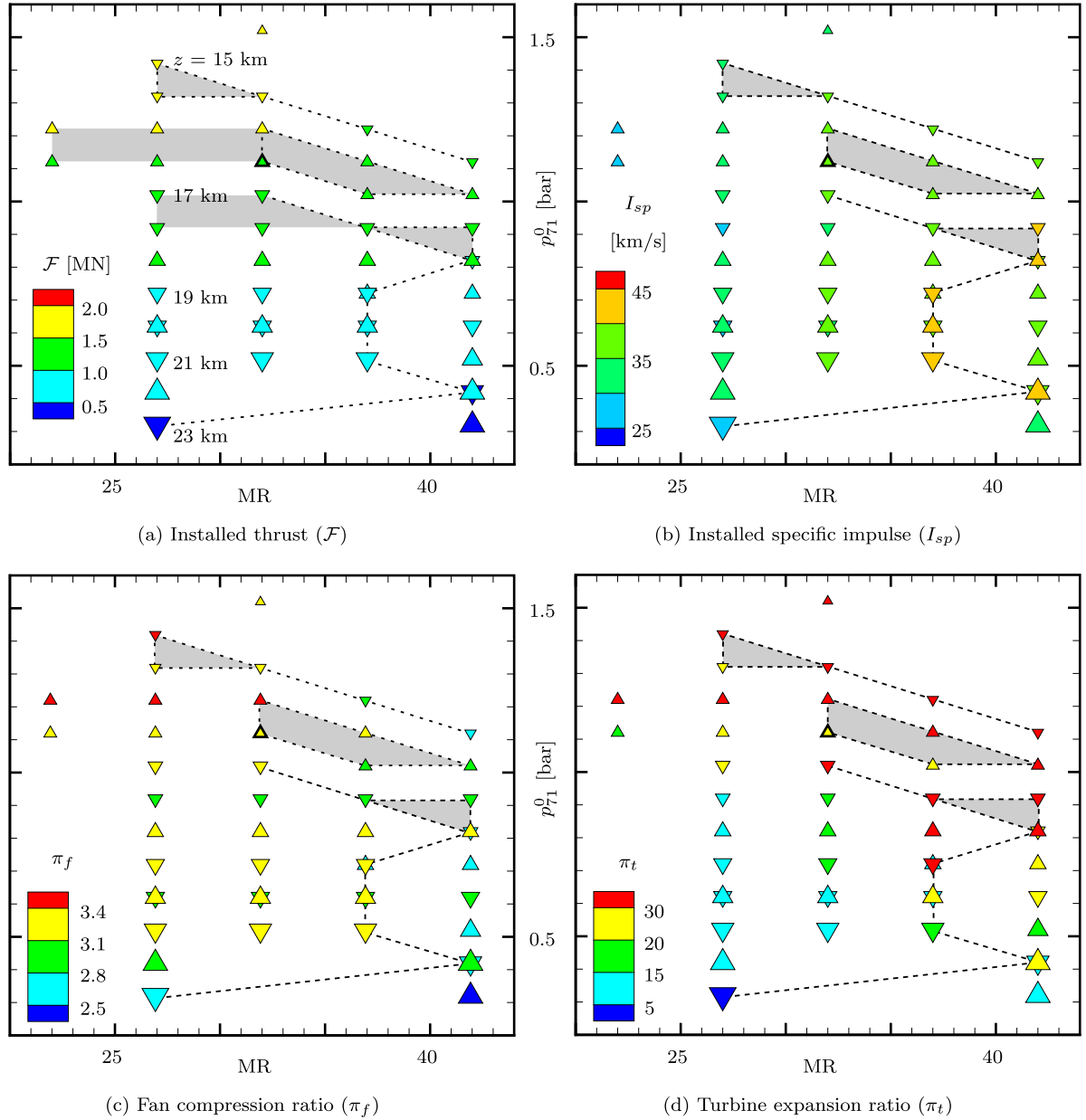
Fig. 14. Operational envelope at $Ma_\infty = 1.5$. Flight altitudes $z = 15, 17, \ldots, 23$ km are indicated with $\triangledown$, whereas $\triangle$ refers to the even values. The symbol size increases with the flight altitude; ($\triangle$) indicates the design point; the dashed lines delimit the optimum operational envelope.

Fig. 18(a) displays the installed thrust and specific impulse while at flight Mach 4. The optimal performance is achieved at each flight altitude throughout the zone of null bleeding ($B < 5\%$) and the air turbo-rockets can be deep-throttled (from 3.4 to 1.6 MN at 19 km). The mission thrust is met without additional compression through the fan above Mach 4. Fig. 19(a) shows installed thrust and specific impulse during flight at Mach 4.5 and constant mixture ratio of 67 in function of the flight altitude and the throat opening. By virtue of Eq. (19), the overall mixture ratio (MR_0) is expressed as:

$$MR_0 = MR \frac{1 - \chi}{(1 - B)\alpha_c^{LSI}}$$

The bypassed flow (B) increases further than the fuel fraction to the dual-mode ramjet (χ), which causes the overall mixture ratio to rise as the throat of the air turbo-rockets closes. As a matter of fact, the throat area of the dual-mode ramjet is fixed and the margin to thermal choke is fairly constant, hence the mixture ra-

tio of the dual-mode ramjet varies barely from 155 at 27 km to 160 at 19 km. Consequently, more air bypasses the combustion chamber of the air turbo-rockets while both the dual-mode ramjet and the air turbo-rockets burn at a constant mixture ratio. In this regime, the propulsion plant is throttled varying the throat area of the air turbo-rockets. Fig. 19(b) reveals that the installed specific thrust and impulse are quite insensitive to the mixture ratio and the flight altitude; the operational point set by the throat opening (A_{81}).

5. Conclusions

An air turbo-rocket expander was conceived, in combination with a dual-mode ramjet, as the propulsion plant of a Mach 8 cruise aircraft. The installed performance of the air turbo-rocket was computed in the velocity range from Mach 1.5 to 4.5 by means of a numerical model comprising the vehicle-integrated intake and nozzle, the dual-mode ramjet and the regenerator. The
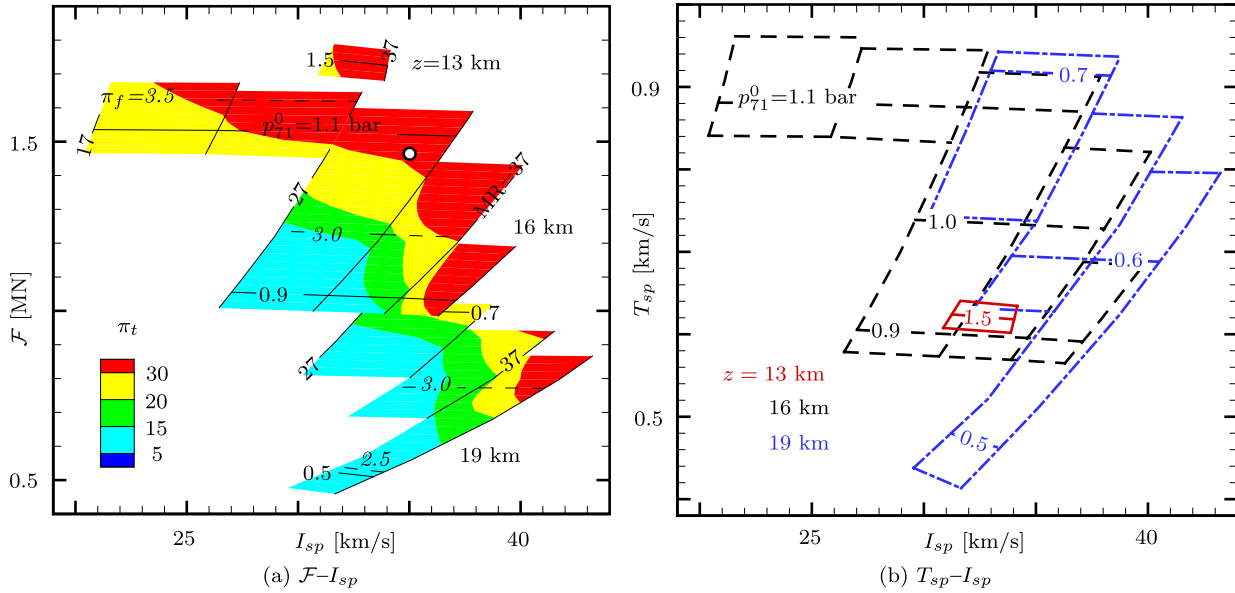
Fig. 15. Installed thrust ($\mathcal{F}$), specific thrust (T_{sp}) and specific impulse (I_{sp}) at $Ma_\infty = 1.5$ and altitudes $z = 13, 16$ and 19 km; (◦) indicates the design point.
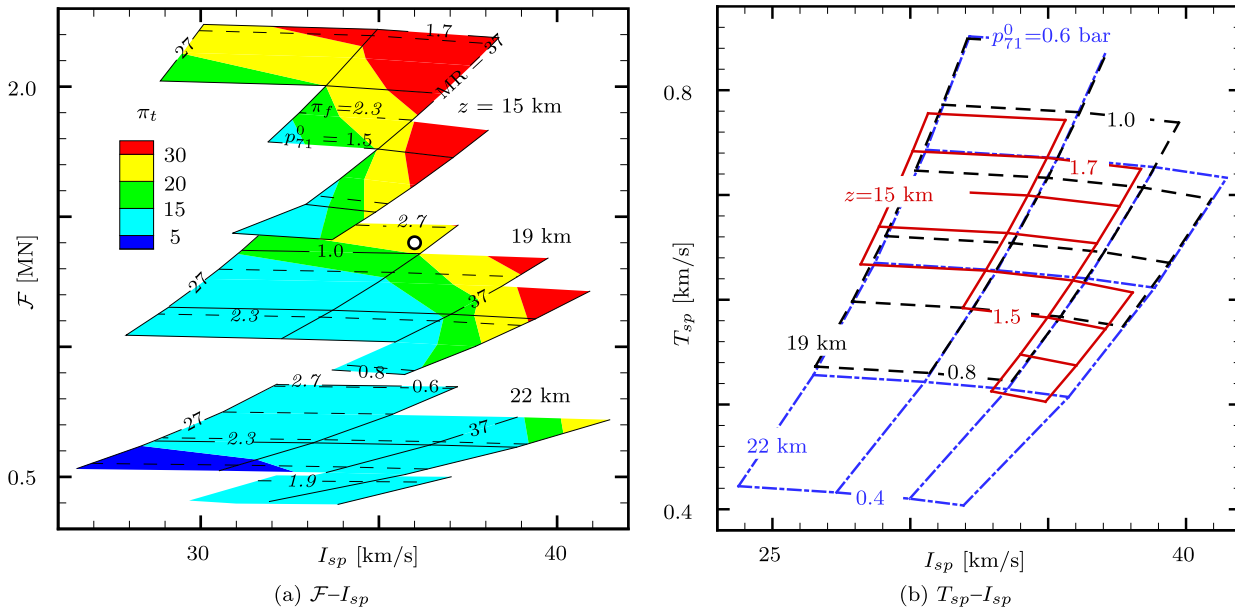

Fig. 16. Installed thrust ($\mathcal{F}$), specific thrust (T_{sp}) and specific impulse (I_{sp}) at $Ma_\infty = 2.0$ and altitudes $z = 15, 19$ and 22 km; (◦) indicates the design point.

heat recovery, instead of the pressure loss, showed to be the critical performance figure that drove the geometrical design of the air turbo-rocket regenerator.

The performances of the propulsive plant were computed along the aircraft ascent trajectory. The thrust requirement was maximum below Mach 2 and the fan compression ratio reached a critical value of 3.2 at Mach 1.5, while the air turbo-rocket throat remained fully open. The regenerator heat recovery was computed with classical correlations and amounted to 500 MW in the Mach range from 1.5 to 3.0. Nonetheless, this thermal power does not suffice to limit the expansion ratio across the hydrogen turbine, which reached a peak value of 30 at Mach 1.5 for stoichiometric combustion in the air turbo-rocket. On the contrary, the decrease of fuel flow as the flight approached Mach 4.5 led to the increase of the turbine inlet temperature up to 1400 K. These extreme behaviors highlighted the need of enhancing the heat transfer in the

regenerator, on one hand, and the convenience of limiting the turbine inlet temperature, on the other hand.

The transfer of momentum from the low speed intake to the exhaust of the dual-mode ramjet contributed to reduce the drag of the dual-mode ramjet duct below Mach 2. Nonetheless, the generation of positive thrust was not noticed up to Mach 4, when the increase of fuel injection in the dual-mode ramjet let the thrust of the dual-mode ramjet alone cancel the intake spillage.

The operational envelope of the propulsion plant was obtained in the range of flight speeds from Mach 1.5 to 4.5. At Mach 1.5, the choking of the nozzle section at the point where the by-passed air was re-injected restricted the flight envelope between 13 and 19 km of altitude. The turbine operated at expansion ratios above 15 throughout a large extension of the operational envelope between Mach 1.5 and 2. These operational conditions would require a large number of turbine stages, hence weight, to meet
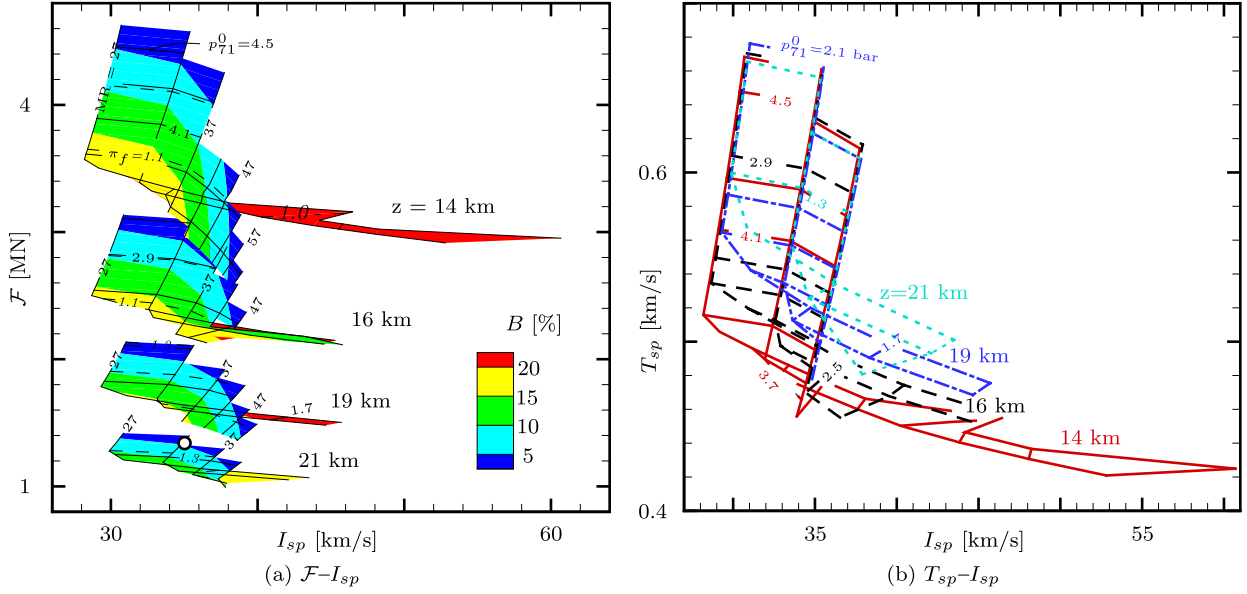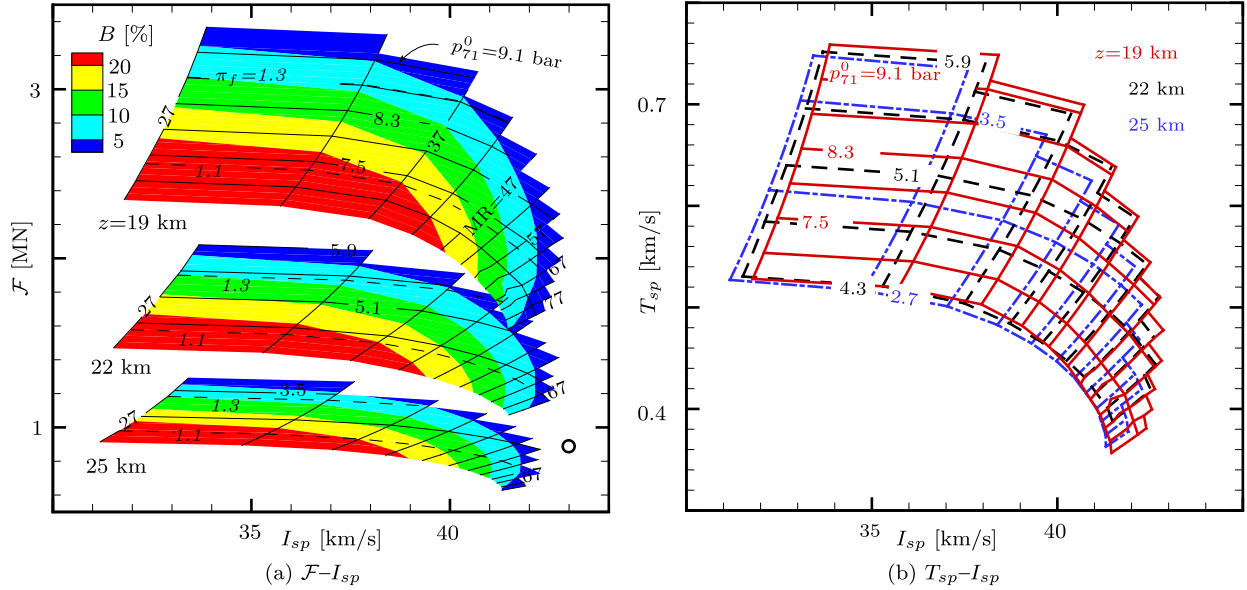
Fig. 17. Installed thrust ($\mathcal{F}$), specific thrust (T_{sp}) and specific impulse (I_{sp}) at $Ma_\infty = 3.0$ and altitudes $z = 14, 16, 19$ and 21 km; ($\circ$) indicates the design point.

Fig. 18. Installed thrust ($\mathcal{F}$), specific thrust (T_{sp}) and specific impulse (I_{sp}) at $Ma_\infty = 4.0$ and altitudes $z = 19, 22$ and 25 km; ($\circ$) indicates the design point.[2]

the targeted turbine adiabatic efficiency of 60%. Nonetheless, this inconvenient can be resolved by enhancing the heat transfer performance across the regenerator and/or reducing the mixture ratio. Therefore engine weight and mixture ratio (or equivalently specific impulse) must be traded-off. The potential detachment of the air turbo-rockets exhaust from the nozzle wall at low altitudes would reduce the thrust and deteriorate the thermal performance of the regenerator, which is critical for the design of the turbine. The three-dimensional flow field within the nozzle was computed with a Navier–Stokes solver using the Spalart–Allmaras one-equation eddy viscosity model [15]. The numerical solution showed that the model assumptions are justified during flight at Mach 3. Nonetheless, this needs to be further assessed at lower flight speeds and altitudes.

At Mach 4, the propulsion plant exhibited optimal performance once the air demand by the turbo-rockets matches the intake mass flow capture. The air turbo-rocket could be deep-throttled (from 3.4 to 1.6 MN at 19 km) varying the mixture ratio and the fan

compression ratio along the line of null bleeding. Above Mach 4, the operational envelope was not limited by the amount of by-passed flow that can be re-injected within the nozzle. In consequence, the specific performances, i.e. installed specific impulse and thrust, were independent of the flight altitude. At Mach 4.5, the turbo-rockets, operating as ram-burners, were throttled varying the throat opening which, in turn, adjusted the bypassed flow. In this regime, the specific impulse and thrust were rather insensitive to the mixture ratio of the air turbo-rocket chamber.

The present study proved the air turbo-rocket expander engine capable of accelerating the Mach 8 cruise aircraft in the supersonic regime, from Mach 1.5 to 4.5, before the dual-mode ramjet takes over. The complexity of the numerical simulation was mo-

---

[2] The convergence of the calculations is very sensitive to the sampling step (Table 7) in the vicinity of the design point. A finer sampling, hence higher computational cost, is required to extend the envelope edge up to the design point.
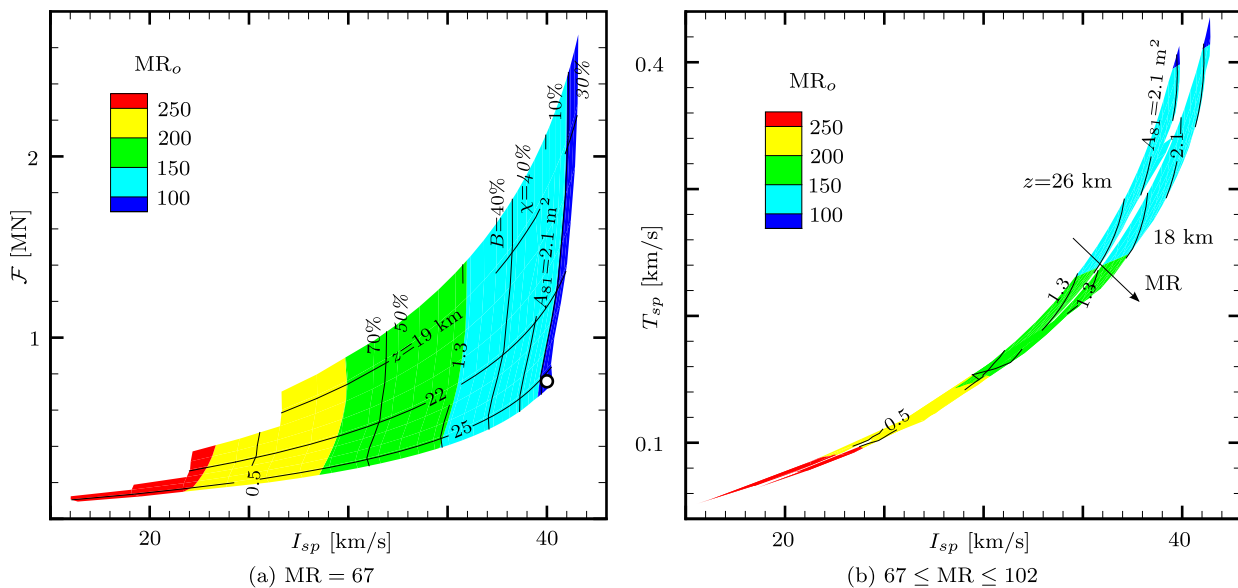
Fig. 19. Installed thrust ($\mathcal{F}$), specific thrust (T_{sp}) and specific impulse (I_{sp}) at $Ma_\infty = 4.5$ and $\pi_f = 1$ and altitudes (z) from 18 to 26 km; ($\circ$) indicates the design point.

tivated by the interaction between the different elements of the propulsion plant, i.e. intakes, turbomachinery, combustion chamber, nozzle, etc. These components obeyed an engineering model formulation. More detailed computational calculations or experimental evaluations could eventually be required to assess the overall or component performances. This is the case of critical components like the airframe-integrated nozzle, where the exhausts of the dual-mode ramjet and the air turbo-rockets mix, or the regenerator, where the heat transfer was computed from classical heat transfer correlations. In line with this, the determination of the characteristics of the intakes below the flight Mach number of 1.5 would allow to evaluate the transonic/subsonic performance of the propulsion plant. Finally, the computations showed that the current re-injection point of the bled air imposed a limit to the altitude during the Mach 1.5 flight. If this would impede the performance of the vehicle, a re-injection at a location further downstream would alleviate the impact and widen up the flight corridor.

Acknowledgements

References

[1] M. Barrére, A. Jaumotte, B. Fraeijs de Veubeke, J. Vandenkerckhove, Rocket Propulsion, Elsevier Publishing Company, 1960.

[2] D.R. Bartz, Turbulent boundary-layer heat transfer from rapidly accelerating flow of rocket combustion gases and of heated air, Adv. Heat Transf. 2 (1965) 1–108, http://dx.doi.org/10.1016/S0065-2717(08)70261-2.

[3] A. Bejan, A.D. Kraus, Heat Transfer Handbook, John Wiley & Sons, Hoboken, NJ, ISBN 0-471-39015-1, 2003.

[4] N.C. Bissinger, N.A. Blagoveshchensky, A.A. Gubanov, V.N. Gusev, V.P. Starukhin, N.V. Voevodenko, S.M. Zadonsky, Improvement of forebody/inlet integration for hypersonic vehicle, Aerosp. Sci. Technol. 2 (1998) 505–514, http://dx.doi.org/10.1016/S1270-9638(99)80009-1.

[5] J. Bossard, M. Thomas, The influence of turbomachinery characteristics on air turbo rocket engine operation, in: Joint Propulsion Conferences, American Institute of Aeronautics and Astronautics, 2000.

[6] M. Bouchez, B. Le Naour, C. Wilhemi, K. Bubenheim, M. Kuhn, J. Riccius, C. Davoine, J.-F. Justin, J. von Wolfersdorf, M. Abdelmoula, J. Steelant, Combustor and material integration for high speed aircraft in the European research program ATLLAS2, in: AIAA Aviation and Aeronautics Forum and Exposition, American Institute of Aeronautics and Astronautics, 2014, in preparation.

[7] S.W. Churchill, Friction-factor equation spans all fluid-flow regimes, Chem. Eng. 84 (1977) 91–92.

[8] S.W. Churchill, R. Usagi, A general expression for the correlation of rates of transfer and other phenomena, AIChE J. 18 (1972) 1121–1128, http://dx.doi.org/10.1002/aic.690180606.

[9] F. Di Matteo, M. De Rosa, M. Onofri, Start-up transient simulation of a liquid rocket engine, in: Joint Propulsion Conferences, American Institute of Aeronautics and Astronautics, 2011.

[10] ESPSS, European Space Propulsion System Simulation, Libraries User Manual, v. 2.4, Empresarios Agrupados International, Madrid, Spain, 2012.

[11] S. Gordon, B.J. McBride, Computer program for the calculation of complex chemical equilibrium compositions with applications, I. Analysis, Technical report RP 1311, NASA, Glenn Research Center, Cleveland, OH, 1994.

[12] G. Hagemann, H. Immich, T. Van Nguyen, G.E. Dumnov, Advanced rocket nozzles, J. Propuls. Power 14 (1998) 620–634, http://dx.doi.org/10.2514/2.5354.

[13] O.J. Haidn, J. Riccius, D. Suslov, S. Beyer, O. Knab, Development of technologies for a CMC-based combustion chamber, Progress Propuls. Phys. (2009) 645–658, http://dx.doi.org/10.1051/eucass/200901645.

[14] W.H. Heiser, Hypersonic Airbreathing Propulsion, American Institute of Aeronautics and Astronautics, ISBN 1563470357, 1994.

[15] Institute of Aerodynamics and Flow Technology, German Aerospace Center (DLR), The DLR TAU Code, http://tau.dlr.de/, 2012.

[16] M. Joly, T. Verstraete, G. Paniagua, Integrated multifidelity, multidisciplinary evolutionary design optimization of counterrotating compressors, Integr. Comput.-Aided Eng. (2014), http://dx.doi.org/10.3233/ICA-140463.

[17] C. Kirchberger, A. Hupfer, H.-P. Kau, S. Soller, P. Martin, M. Bouchez, E. Dufour, Improved prediction of heat transfer in a rocket combustor for GOX/kerosene, in: Aerospace Sciences Meetings, American Institute of Aeronautics and Astronautics, 2009.

[18] O. Knab, et al., Advanced cooling circuit layout for the VINCI expander thrust chamber, in: 38th Joint Propulsion Conference & Exhibit, 2002.

[19] V.V. Kozlaykov, System analysis of jet engines of high supersonic flight velocities, Aerosp. Sci. Technol. 1 (1997) 179–182, http://dx.doi.org/10.1016/S1270-9638(97)90028-6.

[20] T. Langener, J. Steelant, P. Roncioni, P. Natale, M. Marini, Preliminary performance analysis of the LAPCAT-MR2 by means of nose-to-tail computations, in: International Space Planes and Hypersonic Systems and Technologies Conferences, American Institute of Aeronautics and Astronautics, 2012.

[21] E.W. Lemmon, M.O. McLinden, D.G. Friend, NIST Chemistry WebBook, NIST Standard Reference Database Number 23, National Institute of Standards and Technology, Gaithersburg, MD, 20899, 2007.

[22] M. Martinez-Sanchez, Liquid rocket propulsion theory, in: F.A.E. Breugelmans (Ed.), Spacecraft Propulsion, number D/1993/0238/407 in VKI LS 1993-01, Von Karman Institute, Rhode-Saint-Genèse, Belgium, 1993.

[23] C. Meerts, J. Steelant, Air intake design for the acceleration propulsion unit of the LAPCAT-MR2 hypersonic aircraft, in: 5th European Conference for Aeronautics and Space Sciences, EUCASS, Munich, 2013.

[24] C. Meerts, J. Steelant, P. Hendrick, Preliminary design of the low speed propulsion air intake of the LAPCAT-MR2 aircraft, in: 7th European Symposium on Aerothermodynamics, number ESA-SP-692 in ESA Special Publications, European Space Agency, ISBN 978-92-9221-256-8, 2011.

[25] J. Moral, R. Pérez Vara, J. Steelant, M. de Rosa, ESPSS simulation platform, in: Space Propulsion 2010, ESA, San Sebastian, Spain, 2010.

[26] L.R. Petzold, DASSL: differential algebraic system solver, Technical report, Sandia National Laboratories, Livermore, CA, 1983.

[27] I. Rodríguez-Miranda, V. Fernández-Villacé, G. Paniagua, Modeling, analysis, and optimization of the air-turborocket expander engine, J. Propuls. Power 29 (2013) 1266–1273, http://dx.doi.org/10.2514/1.B34781.

[28] P. Roncioni, P. Natale, M. Marini, T. Langener, J. Steelant, Numerical simulations of the LAPCAT MR-2 vehicle scramjet engine, in: 21st International Symposium Air Breathing Engines, ISABE-2013-1656, American Institute of Aeronautics and Astronautics, 2013.

[29] J. Steelant, Sustained hypersonic flight in Europe: first technology achievements within LAPCAT II, in: International Space Planes and Hypersonic Systems and Technologies Conferences, American Institute of Aeronautics and Astronautics, 2011.

[30] G.P. Sutton, O. Biblarz, Rocket Propulsion Elements, 7th edition, John Wiley & Sons, Inc., New York, ISBN 0-471-32642-9, 2001.

[31] N. Tanatsugu, M. Oguma, T. Mizutani, T. Yano, Thermal design of a hydrogen heater for an air turboramjet engine, Exp. Therm. Fluid Sci. 10 (1995) 248–257, http://dx.doi.org/10.1016/0894-1777(94)00090-U.

[32] F. Vázquez, J. Jiménez, J. Garrido, A. Belmonte, Introduction to Modeling and Simulation with EcosimPro, ISBN 978-84-8322-682-7, 2010, Madrid, Spain.

[33] T. Verstraete, CADO: a computer aided design and optimization tool for turbomachinery applications, in: 2nd International Conference on Engineering Optimization, Technical University of Lisbon, Lisbon, Portugal, 2010, number 1297.

[34] Q. Zong, J. Wang, B. Tian, Y. Tao, Quasi-continuous high-order sliding mode controller and observer design for flexible hypersonic vehicle, Aerosp. Sci. Technol. 27 (2013) 127–137, http://dx.doi.org/10.1016/j.ast.2012.07.004.